Scientific Research Publishing

Journal of Minerals and Materials Characterization and Engineering, 2025, 13(5), 227-266
https://www.scirp.org/journal/jmmce
ISSN Online: 2327-4085
ISSN Print: 2327-4077

Investigation of Thermal Rate and Fracture Stress of a Bio-Composite Material Based on Clay and Bone Ash

Mahonde[1], Anyi Joseph Nkongho[1,2,3*], Theodore Tchotang[1]

[1]Department of Mechanical Engineering, National Advanced School Polytechnics of the University of Yaoundé I, Yaoundé, Cameroon
[2]Department of Mechanical Engineering, Higher Technical Teachers Training College of the University of Buea in Kumba, Kumba, Cameroon
[3]Laboratoire de Mécanique et Matériaux (LMM), Ecole Nationale Supérieure Polytechnique de Douala, Université de Douala, Douala, Cameroon
Email: *nkongho.anyi@ubuea.cm

How to cite this paper: Mahonde, Nkongho, A.J. and Tchotang, T. (2025) Investigation of Thermal Rate and Fracture Stress of a Bio-Composite Material Based on Clay and Bone Ash. *Journal of Minerals and Materials Characterization and Engineering*, **13**, 227-266.
https://doi.org/10.4236/jmmce.2025.135014

Received: July 25, 2025
Accepted: September 21, 2025
Published: September 24, 2025

Abstract

This study examines the mechanical and thermal behavior of ten ceramic formulations (C1 to C10) prepared from two types of specimens: Cylindrical Pure clay Specimens (CPC-SP) and Bone Ash Clay Specimens (BAC-SP). The raw materials, sourced from the Missole II clay formation (Douala, Cameroon), were homogenized at room temperature and compacted into cylindrical molds with 10 % water to ensure adequate plasticity and shaping. A total of 100 specimens (five replicates per formulation) were produced under a load of 8.8 N to ensure statistical reliability. Firing experiments, conducted between 750 and 1250˚C, showed that BAC-SP specimens retained 3% residual moisture and exhibited superior mechanical performance, with an average Young's modulus of 6.6 GPa and a fracture stress of 2.56 MPa, compared with 3.56 GPa and 1.66 MPa for CPC-SP. A weight loss on ignition between 1.8 and 2% was recorded in the range of 1120 to 1144˚C, while Poisson's ratio remained constant at 0.5 for both materials. The incorporation of bovine bone ash significantly enhances the strength and thermal stability of ceramics, offering promising opportunities for optimizing firing conditions and extending their use in advanced technological applications.

Keywords

Fracture Stress, Thermal Properties, Bio-Composite Material, Clay, Bone Ash

1. Introduction

Missole II is located in the eastern part of the Douala sub-basin in Cameroon, Central Africa, between latitudes 3˚59' and 3˚54' N and longitudes 9˚54' and 9˚58' E. It is situated in a cold equatorial climate zone. The annual rainfall varies between 3000 and 5000 mm, and the average annual temperature is 26˚C [1]. The geomorphology of the area under study is that of the low-altitude (40 to 120 m) coastal plain of Cameroon. The Missole II area features hills with flat and pointed peaks, which are deeply dissected by the V- and U-shaped valleys of the region's main rivers: the Mbongo, Bongougou, Missolo and Bongo. According to the geological map in the SNH/UD report [2], the Missole II sediments are Paleocene-Eocene in age, corresponding to the N'Kapa Formation (**Figure 1**) [2] [3]. Clay-rich materials are used in the manufacture of ceramics and building materials. However, clay deposits are categorised as sedimentary, alluvial or residual. Knowledge of their occurrence, quantity and properties is necessary for their effective exploitation. Several stratigraphic studies in the Douala sub-basin (southern Cameroon, Central Africa) have shown clay deposits in various formations, the main ones being the Mundeck, Logbadjeck, Logbaba, N'kapa, Matanda, Souellaba and Wouri formations [4]-[6]. The aim is to set up industrial units for manufacturing building materials and ceramics [7], or for exploiting the mineralogical, chemical and thermal properties of clay sediments [8] [9]. Materials made from clay powders are studied and used in a range of applications in materials science and industry, from sophisticated machine parts to everyday items such as porcelain tableware. The versatile use of this class of materials is a consequence of their many useful properties. This class of materials is versatile due to its many useful properties, including its electrical and mechanical properties, and its abundance in nature. In the Missole II area (Douala sub-basin), a study was conducted to locate and describe clay material outcrops and their origin [10]-[12]. Some authors have also demonstrated the potential for producing high-quality ceramic building materials by blending silica, feldspar, kaolinite, and illite clays sourced from the Missole II region [13]-[15].

However, despite preliminary work carried out in the field to describe the clay materials and determine the evolution of their sedimentation [16] [17]. Improving the plasticity of clay requires increasing its grinding cycle, which also improves its granulometry.

In the face of current environmental challenges linked to climate change and resource depletion (United Nations Environment Programme, 2016), the construction and building sector must renovate practices and design methods while taking into account economic health and comfort criteria. However, scientific studies must be carried out on this material to define the conditions for industrial-scale manufacturing, as well as the implementation and maintenance precautions. Despite its many ecological, thermal and economic advantages, raw earth deteriorates under the effect of climatic conditions [18] [19]. It is therefore essential to take precautions to increase its durability. The objective of this work is to contrib-

ute to the improvement of techniques for elaborating ceramic materials based on bovine bone ash. To obtain a homogeneous product of good quality, control the compaction effort of the material to be made in order to reduce the maximum porosity. Respecting the different firing temperature ranges is key in the field of ceramic materials. To achieve the desired outcome, compression tests must be performed on Cylindrical Specimens (CPC-SP and BAC-SP), and the cooking temperature ranges and humidity levels must be observed. The various mechanical characteristics sought are detailed in Section 2 of this paper.

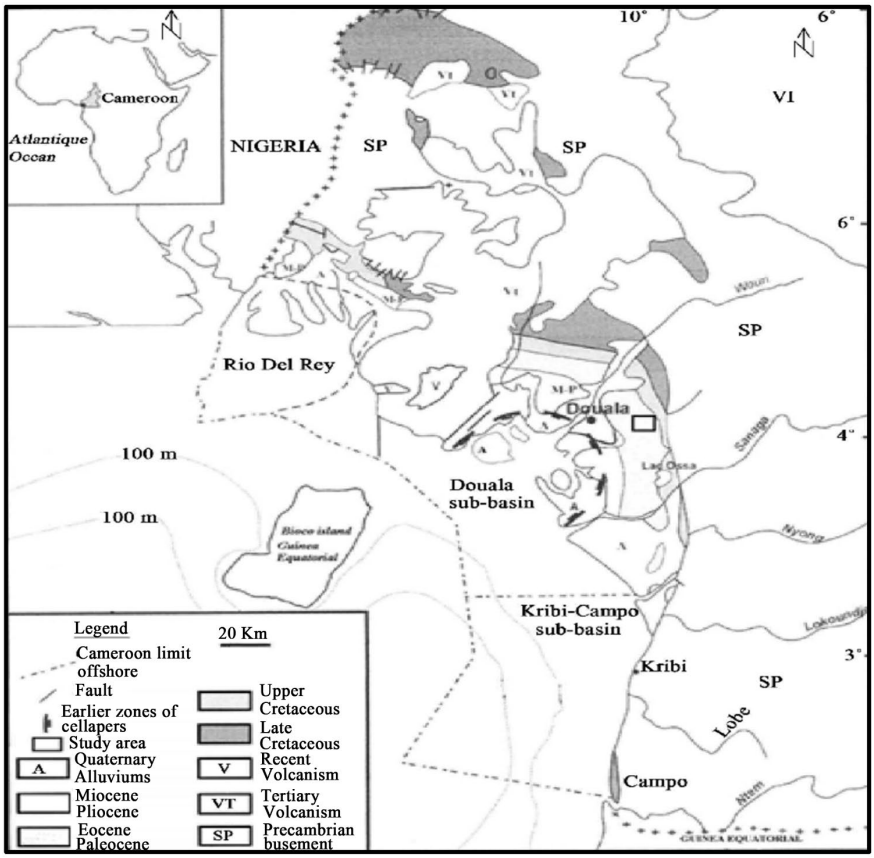

Figure 1. Geological chart of Cameroon's coastal basins. (Source: SNH/UD, 2005)

2. Materials and Methods

The objective of this paragraph is to take five kilograms of clay from the Missole II deposit and produce two types of cylindrical specimens. Cylindrical pure clay specimens (CPC-SP, 15 × 30 mm^2) and cylindrical bone ash clay specimens (BAC-SP, 15 × 30 mm^2) are produced and then assessed.

2.1. Materials

2.1.1. Clay, Kaolin and Bone Ash

The raw materials used in this study consist of four clay profiles representative of the Missole II zone, three profiles from the interfluves along the Douala-Edéa road, and one profile from drilling in the pit on the lower slope of the valley [20]-

[22]. Four clay faces with different mixed textures, such as sandy clay, clayey silt and limo clay, are mainly of sedimentary origin [23] [24]. The average thickness of the exploitable layers is 2.5 m. Two clay samples were taken from the clay layer of each profile, which were representative of mineralogy and chemistry. These data were combined to create an average sample, which was then used for the geotechnical analyses. A sufficient amount of the single mixture (2 - 3 kg of sediment) is collected from a one-metre-long furrow. Sedimentometry is a test that completes the particle size analysis by sieving. This method applies to particles with a diameter of less than 80 micrometres, and the NFP 94-057 standard is recommended for this operation. The mesh size of the sieves used is between 0.1 and 0.002 mm [25] [26]. Clay materials are classified using the Autret method [27] [28]. Bone ash is obtained from waste recovered from bovine bone carcasses, which is then incinerated and crushed according to the particle size recommended by the standard (see **Figure 2**).

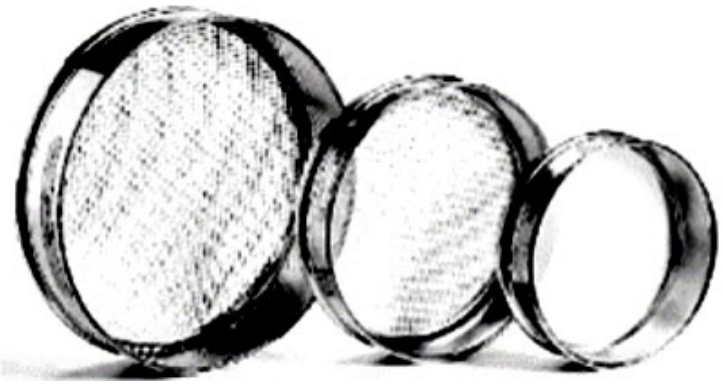

Figure 2. A sieve to obtain different grain sizes.

2.1.2. Tested Pieces

The material is obtained from a mixture of three powders: clay, kaolin, and bone ash. The proportions are presented in **Table 1** for cylindrical BAC-SP (Bone Ash Clay Specimens) and CPC-SP (Pure Clay Specimens) pieces.

Table 1. Volume fractions of components in samples' formulations.

Material	Volume fraction									
	C1	C2	C3	C4	C5	C6	C7	C8	C9	C10
Bone ash (%)	50	50	60	80	40	30	40	50	35	45
Clay (%)	20	15	20	10	30	15	15	25	20	25
Kaolin (%)	15	20	10	5	15	15	30	15	25	15
Water (%)	15	15	10	5	15	40	15	10	20	15
Total (%)	100	100	100	100	100	100	100	100	100	100

With (C1, C2, C3, C4, C3, C5, C6, C8, C9, and C10) representing the different combinations of five replicates each.

2.1.3. Granulometry of Raw Materials

a) Clay

The clay was extracted using a digger and a trowel to facilitate extraction, before being placed in a garbage bag. It should be noted, however, that this clay (see **Figure 3**) is found in solid ground and is devoid of impurities such as dead leaves, pieces of wood, and straw. The contents of the bag were then tipped out to continue the process of sieving. Powder diffractograms of ground bulk samples down to less than 80 μm revealed that the clay materials are kaolinitic and illitic, and allowed the following mineral phases to be detected: kaolinite, quartz, illite, goethite, hematite, and accessory feldspar and anatase [29]-[31]. The particle size required to prepare the powders was obtained using a sieve with mesh sizes ranging from 0.1 to 1 mm.

Figure 3. Raw clay from the quarry.

b) Kaolin

Kaolin, as shown in Figure 4, is one of the most widely used industrial minerals, with global production exceeding 25 million tonnes [32]. While it is used in the production of paper, which accounts for around 75% of global consumption, kaolin is also widely used in the ceramics, rubber, paint, plastics and pharmaceutical industries [33] [34]. Particle size analysis determines the dimensional distribution of grains in an aggregate with dimensions between 0.063 and 125 mm. The mesh sizes and number of sieves are chosen according to particles and the required level of precision. The current standard (EN 933-2) recommends the following calliper of sieves for particle size analysis: 0.063, 0.125, 0.25, 0.50, 1.00, 2.00, 4.00, 8.00, 16.00, 31.50, 63.00 and 125.00. For laser granulometry, bulk kaolin samples and the 40 μm fraction (10 g) were ultrasonically disaggregated and analysed for size using a Master Sizer IP laser granulometer with a displayed size range of 0.1 to 80 μm. This was combined with the Malvern Digital Data Acquisition System at the HydrASA laboratory of the University of Poitiers, France [35]-[37].

c) Bovine Bone Ash

Cattle bone waste (10 kilograms) is collected from cattle slaughterhouses in

Douala. It is then cleaned with hot water to eliminate impurities such as grease, odours, marrow, and other substances that cause nausea. This makes the bone waste clean and suitable for use. After this phase, the bone ash is dried in the open air. After drying, a firing operation (incineration) is carried out in an open-air oven. Complete cooling is obtained after four hours. It should be noted that the cooling time depends on the quantity of bone ash loaded. The desired powder is obtained using a cereal crushing machine see **Figure 5** below [38]-[41].

Figure 4. Raw kaolin.

Figure 5. Bone ash.

2.1.4. Risks of Contamination

There is no risk of contamination when shaping powders. However, we experienced some technical difficulties when developing bovine bone powder. Initially, we opted to use a crushing stone, but subsequently realised that this was difficult, hence the need to use a crusher.

After complete homogenisation, the mixture is introduced into a cylindrical mould coated with a refined oil film, with a diameter of 15 mm and a height of 30 mm. The mixture is then compacted under a maximum axial pressure of 0.05 MPa (see **Figure 6**). This compression occurs between two trays that move slowly at a speed of 0.5 mm/s. This compaction process removes the air in cavitation from the mixture to ensure the cohesion of the constituent elements, the main purpose of which is to produce a sample of constant density. Demoulding takes place at

least two hours after compression to avoid premature deformation of the test pieces (Figure 7).

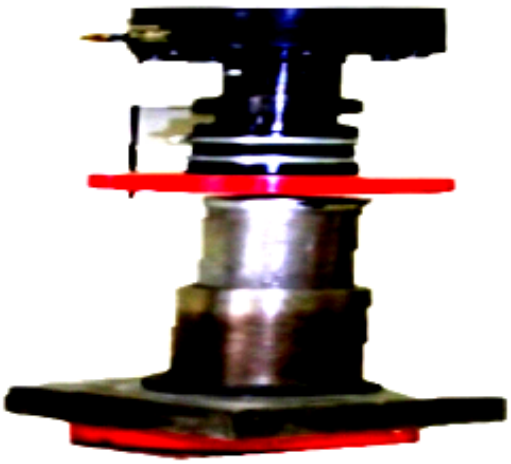

Figure 6. Compaction press.

Figure 7. Unmoulded specimens.

2.2. Methods

2.2.1. Heat Treatment

During heating, clay minerals transform into new, unhydrated minerals. This transformation is a qualitative function of the energy provided. Thus, as the temperature increases, the atoms in the initial crystal lattices change position, allowing other configurations to form. The new phases and state of equilibrium are acquired more quickly the higher the temperature [42]-[44]. At around 800˚C, the initial crystalline phase of the minerals disappears to make way, in varying proportions, for an amorphous phase and new minerals. This is accompanied by shrinkage. Solid reaction, which is associated with changes in porosity and particle dimensions (see Figure 8 and Figure 9), shows the cooking curves of the BAC-SP and CPC-SP. The samples undergo transformations at a temperature of 650˚C and stabilise at 1000˚, 1100˚, and 1300˚C, after which cooling begins. The oven is opened after complete cooling to avoid destroying the samples [45]-[47].

Figure 8. Heated pieces.

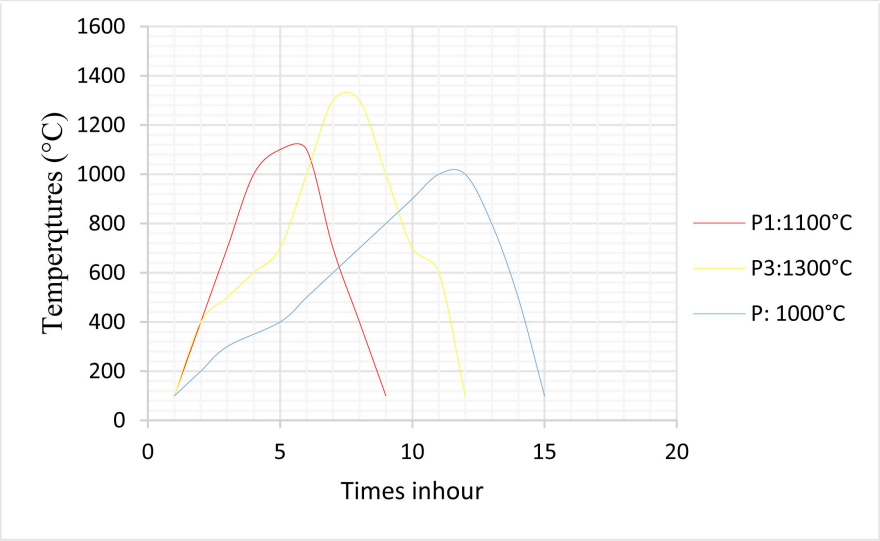

Figure 9. Temperature curves.

2.2.2. Processing

A square sensor on the back of the device sends and receives low-intensity electromagnetic signals through the material being tested. The display shows the relative humidity of the material (% RH) at a maximum depth of 20 mm. The result is more affected by surface moisture than by deep moisture. The MO280 hygrometer is a self-calibrating device, and no other form of calibration is required. These results were achieved using a device called a non-invasive hygrometer. The maximum thickness of the sample to be tested is 3/4 (20 mm). Stack them if they are thin to ensure accurate readings.

2.2.3. Compression Test

This test determines the tensile strength of the specimen (see Figure 10). A force is applied to the cross-section until the specimen cracks in order to determine the stress at fracture.

$$\sigma_{rup} = \frac{F_{\max}}{S} \tag{2.1}$$

where σ_{rup} denotes the stress at fracture, $F_{\max}$ is the maximum applied compression force and S is the initial cross-section. The monitoring of the deformation within the specimen is done using an extensometer equipped with a sensor to determine the Young's modulus,

$$\sigma = E\varepsilon \tag{2.2}$$

$$\varepsilon = \frac{\Delta l}{l_0} \tag{2.3}$$

where σ denotes the axial stress in a specimen, E is the Young's modulus, ε is the axial strain in a piece, Δl is the length variation in mm and l_0 the initial length of a piece.

The compaction test shall be carried out at a low and constant load rate under an imposed stress. The test pieces must be rectified; *i.e.*, the faces in contact with the loading instruments must be smooth to optimise the parallelism of the specimen.

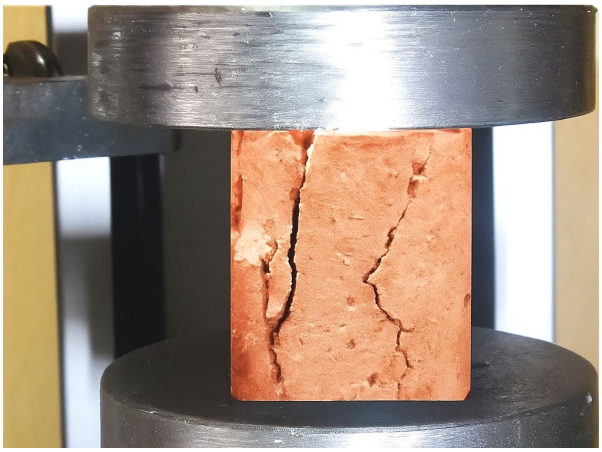

Figure 10. Compression test cylindrical sample of 15 × 30 mm^2.

3. Results and Discussion

3.1. Heat Treatments

Heating clay products is the most important stage. The cooling process must be controlled so that the products release heat at a quasi-constant rate, in order to avoid deformation and maintain directional stresses. The BAC-SP specimens exhibited outstanding classification performance; the C10 combination achieved the best results, followed by combinations C8, C1, and C5. The CPC-SP specimen also demonstrated overall satisfactory performance. The C4 combination stood out by achieving the best results, while the C8, C5, and C1 combinations exhibited slightly

lower performance. The Young's modulus and fracture constraint histograms confirm these rankings (see figure in Appendix).

3.2. Compression Test

Plotting the stress-strain curves of the CPC-SP and BAC-SP specimens made it possible to determine and evaluate their respective Young's modulus values. These curves are illustrated in the appendices. As can be seen at the end of the stress-strain curve plots, the specimens based on bone ash clay samples highlight the difference compared to pure clay (BAC-SP). This is presented in the Appendix. The BAC-SP specimens have a modulus E between 1.30 and 3.50 GPa, with low breaking stress values. Therefore, it appears that the C3 and C6 combinations present average values of Young's modulus. However, the respective Young's modulus values of the CPC-SP specimens are [1.05; 3.56] GPa, with low breaking stress values. The graphs in Appendix illustrate the results of the different Young's moduli of the BAC-SP and CPC-SP specimens. It should be noted that the compaction process achieved perfect cohesion of the constituent elements. The way the grains are stacked plays a major role in the quality and mechanical strength of the raw specimen. The conditions used to prepare the specimens are similar to those used for industrial tiles (water content: $\omega = 20\%$; density: $\rho = 2$ g/cm^3). All specimens were developed under the same experimental conditions using powders from three varieties. The kneaded product is introduced manually into the moulding cylinder; the quantity of dough introduced determines the density after compaction, $\rho = 2$ g/cm^3. The volume of dough to be introduced is defined by $m = \rho V$; with $V = \pi \times D^2 \times h/4$ for a (cylindrical specimen. The dimensions (diameter: $D = 15$ mm; height: $h = 30$ mm) are such that uniform compaction is achieved throughout the thickness of the specimen.

A compaction force of 8.5 kN is applied to produce a homogeneous, compact product. This compaction (see **Figure 10**) also eliminates air bubbles and prevents the formation of pockets in the material, which can lead to sudden rupture and distort the experimental results.

3.3. Humidity

Measurements are carried out using a non-invasive hygrometer (model MO280), which requires the samples to be stable for precise results. **Table 2** summarises the different cooking temperature ranges and the recorded humidity levels of all BAC-SP and CPC-SP formulations. Regarding BAC-SP specimens, we recorded values ranging from 1.2% to 4.9%. CPC-SP specimens exhibit values ranging from 0.3% to 4.08%, with the C9 and C10 formulations reaching 4.08%. Increasing the cooking temperature significantly improves the likelihood of achieving defect-free samples with an optimal surface finish [48]-[50]. It is found that specimens made from bone ash are stiffer than those made from pure clay; several technical factors account for this enhancement in stiffness:

Table 2. Humidity rates and heating temperature of BAC-SP and CPC-SP.

Combinations	Pieces	Heating Temperature T (˚C)	Humidity rate TH (%)	Combinations	pieces	Heating Temperature T (˚C)	Humidity rate TH (%)
C1	BAC-SP	1250	1.2	C1	CPC-SP	1250	0.3
C2	BAC-SP	1400	1.8	C2	CPC-SP	1400	1.3
C3	BAC-SP	750	2.1	C3	CPC-SP	750	1.5
C4	BAC-SP	1350	2.2	C4	CPC-SP	1350	1.6
C5	BAC-SP	1100	2.5	C5	CPC-SP	1100	1.7
C6	BAC-SP	1300	3.3	C6	CPC-SP	1300	1.8
C7	BAC-SP	950	3.9	C7	CPC-SP	950	4.6
C8	BAC-SP	1050	4.05	C8	CPC-SP	1050	4.7
C9	BAC-SP	1000	4.09	C9	CPC-SP	1000	4.08
C10	BAC-SP	1050		C10	CPC-SP	1050	

✓ **Mineral composition of bone ash**

Bone ash predominantly consists of calcium phosphate (apatite) along with other mineral oxides [51]. During the firing process, these constituents promote the development of a glassy phase that significantly reinforces the overall microstructure. The resulting mineral phases enhance intergranular cohesion and effectively reduce residual porosity, thereby contributing to increased stiffness of the ceramic material [52].

✓ **High-temperature behaviour.**

At high temperatures, the components of bone ash actively facilitate sintering and improve the bonding between clay particles [53] [54]. In contrast, pure clay tends to remain more porous and exhibits a lower degree of consolidation after firing.

Conversely, the TH (%) BAC-SP > TH (%) CPC-SP rate is higher; it has been observed that specimens made from bone ash exhibit greater stiffness compared with those made from pure clay. This difference is primarily attributed to the composition of bone ash, which is rich in calcium phosphate, particularly in the form of hydroxyapatite. The difference may also be explained by the presence of residual organic matter or more thermally reactive phases in the bone ash. During thermal treatment, these components can lead to a greater release of heat compared with the specimens made from pure clay, which are predominantly mineral and more thermally stable. This compound imparts a denser and more rigid structure to the material, thereby enhancing its overall mechanical properties. Bone ash acts as a ceramic reinforcement agent, promoting the formation of a matrix that is more resistant to deformation [55]. This is simply

because the clay itself contains physical water as well as chemical water, which allows ceramists to knead clay easily. Conversely, the addition of bone ash acts as a degreaser, drawing up a large proportion of the physical water and thereby facilitating implementation.

3.3.1. Measurement of the Masses of Specimens Manufactured before and after Thermal Firing

After manufacturing the test pieces, it is essential to measure their mass before and after firing. The results obtained are shown in the table in the Appendix. After cooking at 1000˚C, low linear shrinkage is recorded due to the small dimensional variation. Shrinkage is high for samples with low compaction effort. This applies to specimen CPC-SP43 of combination C9, as well as specimens CPC-SP36 and CPC-SP37 of combination C8. These parts are less fragile and do not show any cracks or deformations after cooking; however, they exhibit a beige colouring and a perfect surface condition [56]-[58]. Defects that cause brittleness in ceramic materials include macroscopic defects such as porosity and surface defects, as well as microscopic defects such as dislocations, vacancies, and interstitial atoms, and their interactions. Porosity reduces mechanical resistance. Since pores concentrate tension, the best materials from a mechanical point of view are those that are completely dense. The opposite occurs for resistance to thermal shock [59]-[61].

3.3.2. Observations and Interpretations of BAC-SP Specimens

Table 2 summarises the changes to the samples after firing at 1100˚C. We recorded low linear shrinkage for all the samples, except for combinations C1 and C2, which stand out because of their very high kaolin content. Regarding volume shrinkage, it reaches 6.25% for samples with a high clay content; this applies to specimens C3 and C4 [62]-[64]. Samples with a high bone ash content have a better physical appearance than samples with a high kaolin content, which are slightly fragile [65]-[67]. The porosity is low due to the advanced vitreous phase at a higher temperature and the consolidation of materials, which reduces the void volume.

3.3.3. Interpretation of the Tables and Stress-Deformation Stress-Deformation Curves of the Two Specimens

Plotting the stress-deformation curves of the BAC-SP and CPC-SP specimens enables the respective Young's modulus and breaking stress values of each specimen to be determined with accuracy and precision (see the curves in Appendix). To do this, it is necessary to briefly comment on the behaviour and characteristics of each curve. From the comments on all the curves, one can see that the CPC-SP specimens have a higher average Young's modulus than the BAC-SP specimens. The BAC-SP specimens have the highest average breaking stress. They experience higher stress than CPC-SP specimens. When subjected to stress, these specimens break with little or no plastic deformation. This is because fragile materials absorb relatively little energy before breaking, even if they are strong. In

the case of brittle fracture, no apparent plastic deformation takes place before rupture. Cracks spread quickly. Evidence of these results (average breaking stress and average Young's modulus of all samples) is presented in Table 3 below. However, BAC-SP specimens are lighter than CPC-SP specimens.

Table 3. Average failure stresses and average Young's moduli of the specimens (CPC-SP and BAC-SP).

BAC-SP			CPC-SP		
Combination	E_m **[GPa]**	σ_{rm} **[MPa]**	**Combination**	E_m **[GPa]**	σ_{rm} [MPa]
C1	2.05	0.26	C1	2.08	0.15
C2	1.32	0.19	C2	1.05	0.09
C3	2.49	0.37	C3	3.10	0.17
C4	2	1	C4	4	0.31
C5	2.10	0.28	C5		0.29
C6	2.05	1	C6	3	0.36
C7		0.39	C7		0.31
C8	2	0.20	C8	2.06	0.33
C9	2.06	0.32	C9	2	0.20
C10	2.08	0.31	C10	3.49	1

3.3.4. Observations and Interpretations of the Tables

In Table 2, the same temperature range has been set for the two specimens: (BAC-SP) and (CPC-SP). However, at temperatures of 1000˚C to 1050˚C, the C9 and C10 combinations have an equal humidity percentage of around 4.09%, making them the highest values for the BAC-SP specimens. The lowest percentage, around 1.2%, is found in combination C1. It is also noted that, within the temperature range of 1000˚C to 1050˚C, the C9 and C10 CPC-SP specimen combinations have an equal humidity percentage of around 4.08%. The lowest humidity percentage is around 0.3%; this is the case for combination C1. Overall, the humidity rate percentage of the BAC-SP specimens is higher than that of the CPC-SP specimens, indicating that these materials are suitable for producing ceramics.

Table 4 summarises the colour change of CPC-SP specimens after firing, as well as the low linear shrinkage observed in all samples. No cracks were observed, but slight deformations were noted, which did not affect the test results. The lowest percentage of mass variation is around 0.45% for combination C6 and around 1.75% for specimen C1. Volume variation is around 4.21% for the C5 specimens, C6, and C10, and around 0.32% for the C7, C8, and C9 combinations. In terms of fire losses, the lowest percentage is around 0.25% for combination C5 and the highest is around 2.06% for combination C8.

Table 4. Mass measurement table for CPC-SP before and after baking.

	Mass before draying			Mass after draying					Mass after baking	
CPC-SP	M_1 [g]	H_1 [mm]	V_1 [mm^3]	M_2 [g]	H_2 [mm]	V_2 [mm^3]	D_m [%]	D_v [%]	M_3 [g]	Pf
C1	44.85	30.5	5387.0625	44.05	30	5298.75	1.75	1.63	43.53	0.51
C2	44.52	30.5	5387.0625	44.07	30	5298.75	0.98	1.63	43.51	0.56
C3	44.85	31.25	5519.25	43.44	30.25	5342.25	1.19	3.20	43.30	1.53
C4	44.52	31.25	5519.25	43.84	30.25	5342.25	1.38	3.20	43.12	0.78
C5	44.01	30.5	5531.67	43.3	30	5298.75	1.61	4.21	43.04	0.25
C6	43.50	30.5	5531.67	43.30	30	5298.75	0.45	4.21	42.98	0.38
C7	43.66	30.3	5351.73	43.06	30.2	5334.07	1.36	0.32	42.44	0.61
C8	43.78	30.3	5351.73	43.24	30.2	5334.07	1.08	0.32	42.38	2.06
C9	43.82	30.3	5351.73	43.18	30.2	5334.07	1.23	0.32	42.50	1.28
C10	43.72	30.5	5531.67	43.24	30	5298.75	1.07	4.21	42.99	0.31

Table 5 also shows the colour variation of the BAC-SP test pieces after cooking, as well as the average variations in mass and volume of all combinations. The lowest variation in mass is around 0.85% for the C10 combination. The highest average value is around 2.06% for combination C3. The lowest average

Table 5. Mass variation table for BAC-SP before and after firing.

	Initial Mass			Mass after draying					Mass after baking	
BAC-SP	M_1 [g]	H_1 [mm]	V_1 [mm^3]	M_2 [g]	H_2 [mm]	V_2 [mm^3]	D_m [%]	D_v [%]	M_3 [g]	Pf
C1	43.4	31	5475.375	42.46	30	5298.75	2.25	3.22	42.02	0.41
C2	43.44	31	5475.375	42.43	30	5298.75	2.33	3.22	42.02	0.40
C3	43.6	32	5652	42.42	30	5298.75	2.6	6.25	42.14	0.28
C4	43.39	32	5652	42.39	30	5298.75	2.27	6.25	42.12	0.26
C5	42.89	31.5	5563.68	42.35	31	5475.37	1.25	1.58	42.04	0.30
C6	42.95	31.5	5563.68	42.40	31	5475.37	1.26	1.58	42.12	0.28
C7	42.78	30.36	5404.72	42.37	30.5	5387.05	0.94	0.32	42.06	0.22
C8	42.97	30.36	5404.72	42.43	30.5	5387.06	1.25	0.32	42.03	0.39
C9	42.98	31.5	5563.68	42.36	31	5475.37	1.42	1.58	42.03	0.33
C10	42.81	30.36	5404.72	42.44	30.5	5387.06	0.85	0.32	42.01	0.43

M_1: Mass before drying. M_2: Mass after drying. M_3: Mass after cooking. H_1: Height before drying. H_2: Height after drying. V_1: Volume before drying. V_2: Volume after drying. D_v: Volume variation. D_m: Mass variation. Pf: Ignition loss. E_m: Average Young's modulus. σ_{rm} : Average breaking stress.

volume change is around 0.32%; this applies to combinations C7, C8, and C10. The largest average volume variation is around 6.25%; this occurs for combinations C3 and C4. The average percentage ignition loss (Pf) is recorded; the lowest value is around 0.22% for combination C7, and the largest value is around 0.43% for combination C10.

After observing the results in Table 3 and Table 4, it is noted that the two test pieces (BAC-SP and CPC-SP) underwent the manufacturing process provided for by the regulations in force for ceramic products, as the compaction effort ensured that the material was homogeneous and resistant during heat treatment.

$$D_v = \frac{V_1 - V_2}{V_1} \times 100$$

$$D_m = \frac{M_1 - M_2}{M_1} \times 100$$

Table 6 is, in some way, the synthesis of Table 5 and Table 3. Table 3 presents the general results of the Young's moduli and breaking stresses of the two specimens, BAC-SP and CPC-SP. The Young's modulus of BAC-SP is between 1.32 GPa and 2.49 GPa. It is seen that certain combinations have common results; this is the case for C1, C6, and C7: the modulus is of the order of 2.05 GPa. The C2 combination has the lowest result, of around 1.32 GPa, and C3 has the highest result of all the CPC-SP combinations (see Table 7). The other combinations, namely C5, C9, and C10, have modulimodules ranging from 2.06 GPa to 2.08 GPa. We also see that combinations C4 and C8 are equal, the common Young's modulus being of the order of 2 GPa. These materials are light and rigid, not very fragile and have no plastic deformation; they have low breaking stress. Just like the previous case, some combinations of the CPC-SP specimen have common results; this is the case for combinations C4 and C4 and, among others, combinations C6 and C7. Combination C2 has the lowest result, of around 1.05 GPa. Combinations C3 and C10 have results of 3.10 GPa and 3.49 GPa, respectively. The others, C9, C8, and C1 respectively, result in 2 GPa, 2.06 GPa, and 2.08 GPa. The C4 and C5 combinations stand out from all other combinations with a value of 4 GPa. CPC-SP specimens are rigid, not light, and fragile. As compared to the BAC-SP specimens, the breaking stresses of the CPC-SP specimens are lower.

3.3.5. Comparing BAC-SP and CPC-SP Specimens

Despite the reaction of the raw materials to cooking, heat causes changes in density, porosity, hardness, and dimensions. It also causes dehydration, decomposition, and combinations, which modify the mechanical properties [68]-[70]. This leads us to conclude that the specimens we produced are suitable for the production of ceramic products. In fact, this observation can be verified by examining the results of the mechanical tests; CPC-SP specimens are the most effective product. Missole II clay materials are ideal for manufacturing bricks, tiles, and sandstones [71]-[73].

Table 6. Grouping of Young's moduli of BAC-SP pieces.

Specimens C1	E [GPa]	Specimens C3	E [GPa]	Specimens C5	E [GPa]	Specimens C7	E [GPa]	Specimens C9	E [GPa]
BAC-SP1	2.28	BAC-SP11	1.92	BAC-SP21	2.34	BAC-SP31	2.32	BAC-SP41	1.87
BAC-SP2	0.98	BAC-SP12	2.48	BAC-SP22	1.64	BAC-SP32	2.79	BAC-SP42	2.84
BAC-SP3	3.05	BAC-SP13	3.16	BAC-SP23	2.71	BAC-SP33	0.71	BAC-SP43	1.38
BAC-SP4	3.20	BAC-SP14	1.99	BAC-SP24	0.67	BAC-SP34	2.67	BAC-SP44	2.35
BAC-SP5	0.74	BAC-SP15	2.92	BAC-SP25	3.15	BAC-SP35	1.7	BAC-SP45	1.87
E_m = 2.05 GPa		E_m = 2.49 GPa		E_m = 2.10 GPa		E_m = 2.03 GPa		E_m = 2.06 GPa	
Specimens C2	**E [GPa]**	**Specimens C4**	**E [GPa]**	**Specimens C6**	**E [GPa]**	**Specimens C8**	**E [GPa]**	**Specimens C10**	**E [GPa]**
BAC-SP6	1.18	BAC-SP16	2.58	BAC-SP26	2.87	BAC-SP36	2.07	BAC-SP46	1.49
BAC-SP7	0.76	BAC-SP17	2.56	BAC-SP27	2.43	BAC-SP37	1.1	BAC-SP47	3.15
BAC-SP8	1.21	BAC-SP18	1.10	BAC-SP28	5.92	BAC-SP38	0.89	BAC-SP48	2.80
BAC-SP9	1.84	BAC-SP19	0.82	BAC-SP29	2.67	BAC-SP39	1.68	BAC-SP49	1.49
BAC-SP10	1.95	BAC-SP20	0.48	BAC-SP30	3.59	BAC-SP40	2.07	BAC-SP50	1.49
E_m = 1.32 GPa		E_m = 1.50 GPa		E_m = 3.50 GPa		E_m = 1.56 GPa		E_m = 2.08 GPa	

Table 7. Grouping of Young's moduli of CPC pieces.

Specimens C1	E [GPa]	Specimens C2	E [GPa]	Specimens C3	E [GPa]	Specimens C4	E [GPa]	Specimens C5	E [GPa]
CPC-SP1	0.90	CPC-SP6	0.59	CPC-SP11	3.95	CPC-SP16	2.59	CPC-SP21	1.84
CPC-SP2	1.87	CPC-SP7	0.63	CPC-SP12	2.89	CPC-SP17	4.74	CPC-SP22	1.81
CPC-SP3	2.76	CPC-SP8	0.73	CPC-SP13	1.81	CPC-SP18	4.60	CPC-SP23	3.37
CPC-SP4	1.60	CPC-SP9	1.29	CPC-SP14	2.92	CPC-SP19	3.38	CPC-SP24	1.07
CPC-SP5	2.02	CPC-SP10	2.03	CPC-SP15	3.95	CPC-SP20	2.59	CPC-SP25	1.84
E_m = 1.83 GPa		E_m = 1.05 GPa		E_m = 2.64 GPa		E_m = 3.58 GPa		E_m = 1.98 GPa	
Specimens C6	**E [GPa]**	**Specimens C7**	**E [GPa]**	**Specimens C8**	**E [GPa]**	**Specimens C9**	**E [GPa]**	**Specimens C10**	**E [GPa]**
CPC-SP26	3.43	CPC-SP31	2.81	CPC-SP36	1.87	CPC-SP41	2.07	CPC-SP46	2.87
CPC-SP27	3.15	CPC-SP32	1.34	CPC-SP37	2.84	CPC-SP42	1.10	CPC-SP47	2.43
CPC-SP28	2.80	CPC-SP33	2.60	CPC-SP38	1.38	CPC-SP43	0.89	CPC-SP48	5.92
CPC-SP29	3.43	CPC-SP34	3.88	CPC-SP39	2.35	CPC-SP44	1.68	CPC-SP49	2.67
CPC-SP30	1.49	CPC-SP35	2.81	CPC-SP40	1.87	CPC-SP45	2.07	CPC-SP50	2.67
E_m = 2.86 GPa		E_m = 2.68 GPa		E_m = 2.06 GPa		E_m = 1.65 GPa		E_m = 3.32 GPa	

4. Conclusions

In summary, the temperature rise rate, maximum cooking temperature, and holding time essentially depend on the thermal power of the vacuum speed in the furnace. Scrupulously respecting these three factors is essential for determining the mechanical properties, which are one of the targets of this study.

The cooking method has a significant impact on the quality of the cooking. The load must be homogeneous to avoid creating preferential paths. Following the tests carried out, it can be concluded that specimens based on BAC-SP bovine bone ash have appreciable mechanical and thermal characteristics. The mixture of bone ash and clay increases the firing temperature, opening up the possibility of producing refractory materials due to their pyroscopic resistance. The results of the compression tests show that the clay formation in the Missole II zone beneath the Douala basin is suitable for manufacturing building materials and producing porous, low-lustre ceramics. However, an important observation was made regarding the CPC-SP specimens. The very low porosity values mean that the resulting material is not only resistant, but also less fragile. This can generally be attributed to the application of compaction forces during the shaping of the specimens. On the other hand, the variation in the fraction of components in the different combinations is essential for scrupulously respecting the implementation techniques for obtaining a quality final product that respects the geometric, technical constraints, dimensions and surface condition.

The main issue with our manufactured products is their fragility. They are subject to shock and deformation due to the shaping process and to the moisture loss, which loses between 13 and 18% of its volume during the cooking process. Generally, these manufactured products have many advantages because they are resistant to heat and wear, making them durable over time. However, their main disadvantage is fragility. Thanks to their impressive mechanical properties, ceramic products are a staple of the kitchen. The ceramic firing temperature depends on the type of clay and the desired final effect. In order to completely eliminate the brittleness defect, further research must be conducted to solve this major problem of ceramic products.

Acknowledgements

Our thanks go first to my family and then to my supervisors for the success of this research.

Conflicts of Interest

We declare that no competing interests exist.

References

[1] Roberts, P., Hunt, C., Arroyo-Kalin, M., Evans, D. and Boivin, N. (2017) The Deep Human Prehistory of Global Tropical Forests and Its Relevance for Modern Conservation. *Nature Plants*, **3**, 1-9. https://doi.org/10.1038/nplants.2017.93

[2] Logmo, E.O., Ngon, G.F.N., Samba, W., Mbog, M.B. and Etame, J. (2013) Geotechnical, Mineralogical and Chemical Characterization of the Missole II Clayey Materials of Douala Sub-Basin (Cameroon) for Construction Materials. *Open Journal of Civil Engineering*, **3**, 46-53. https://doi.org/10.4236/ojce.2013.32a006

[3] Penka, J.B., Nana, U.J.M.P., Manjia, M.B., Bomeni, I.Y. and Pettang, C. (2022) Hydrological, Mineralogical and Geotechnical Characterisation of Soils from Douala (Coastal, Cameroon): Potential Used in Road Construction. *Heliyon*, **8**, e11287. https://doi.org/10.1016/j.heliyon.2022.e11287

[4] Nguimbous-Kouoh, J.J., Tchutchoua, J., Ngos III, S., Mbarga, T.N. and Manguelle-Dicoum, E. (2018) Hydrocarbon Potential of Two Coastal Basins (Cameroon). *International Journal of Geosciences*, **9**, 131-147. https://doi.org/10.4236/ijg.2018.92009

[5] Mfayakouo, B.C., Ngaha, P.R.N. and Bitom, D.L. (2021) Age and Paleo-Environmental Evolution of the Douala Basin (Cameroon) during the Cenozoic: Insights from Palynology and Sequence Analysis. *Heliyon*, **7**, e08514. https://doi.org/10.1016/j.heliyon.2021.e08514

[6] Mbog, M.B., Ngon Ngon, G.F., Tassongwa, B., Tehna, N., Tedontsah, V.P.L. and Etame, J. (2022) Clay Deposits of Ngoma (Douala Sedimentary Subbasin Cameroon, Central Africa): A Provenance Study. *Arabian Journal of Geosciences*, **15**, Article No. 1122. https://doi.org/10.1007/s12517-022-10130-5

[7] Fugazzotto, M., Mazzoleni, P., Lancellotti, I., Camerini, R., Ferrari, P., Tiné, M., *et al*. (2023) Industrial Ceramics: From Waste to New Resources for Eco-Sustainable Building Materials. *Minerals*, **13**, Article No. 815. https://doi.org/10.3390/min13060815

[8] Yanti, E.D. and Pratiwi, I. (2018) Correlation between Thermal Behavior of Clays and Their Chemical and Mineralogical Composition: A Review. *IOP Conference Series: Earth and Environmental Science*, **118**, Article ID: 012078. https://doi.org/10.1088/1755-1315/118/1/012078

[9] Geng, J. and Sun, Q. (2018) Effects of High Temperature Treatment on Physical-Thermal Properties of Clay. *Thermochimica Acta*, **666**, 148-155. https://doi.org/10.1016/j.tca.2018.06.018

[10] Bukalo, N.N., Ekosse, G.-I., Odiyo, J. and Ogola, J. (2020) Geochemistry and Possible Industrial Applications of Cretaceous-Tertiary Kaolins of the Douala Sub-Basin, Cameroon. *Periodico di Mineralogia*, **89**, 225-242.

[11] Bayiga, E., Ntamak-Nida, M., Etame, J., et al. () Trace Elements Geo-Chemistry of Clay Deposits of Missole II from the Douala Sub-Basin in Cameroon (Central Africa): A Provenance Study. *Sciences, Technologie & Développement*, **13**, 20-35.

[12] Sobdjou, C.K., Mfayakouo, B.C., Ngueutchoua, G., Kenfack, R.G.N. and Ngos, S. (2023) Palaeoenvironment of the Albian-Cenomanian Mundeck Formation in the Douala Basin (SW, Cameroon): Evidence from Facies Analysis and Geochemistry. *Geological Journal*, **58**, 2057-2077. https://doi.org/10.1002/gj.4710

[13] Njoh, O.A. and Sama, N. (2022) Palynostratigraphy of the Paleocene-Eocene Shallow Marine Petroleum Source Rock Sections, Outcropping in Missole, Nkapa Formation, Douala/Kribi-Campo Basin, Cameroon.

[14] Bodvarson, G.S., Pruess, K. and Lippmann, M.J. (2023) Numerical Evaluation of Geothermal Systems. *Brazilian Journal of Geophysics*, **5**, 311-318. https://doi.org/10.22564/brjg.v5i2.2249

[15] Nugraha, R., O'Sullivan, J., O'Sullivan, M. and Abdurachman, F. (2022) Geothermal

Modelling: Industry Standard Practices. 47*th Workshop on Geothermal Reservoir Engineering*, Stanford, 7-9 February 2022, 1-12. https://pangea.stanford.edu/ERE/pdf/IGAstandard/SGW/2022/Nugraha.pdf

[16] Waleed, M. and Alshawmar, F. (2025) Enhancing Mechanical Properties of Low Plasticity Soil through Coal and Silica Fume Stabilization. *Scientific Reports*, **15**, Article No. 9990. https://doi.org/10.1038/s41598-025-94149-0

[17] Moreno-Maroto, J.M. and Alonso-Azcárate, J. (2018) What Is Clay? A New Definition of "Clay" Based on Plasticity and Its Impact on the Most Widespread Soil Classification Systems. *Applied Clay Science*, **161**, 57-63. https://doi.org/10.1016/j.clay.2018.04.011

[18] Yang, M., Chen, L., Wang, J., Msigwa, G., Osman, A.I., Fawzy, S., *et al*. (2022) Circular Economy Strategies for Combating Climate Change and Other Environmental Issues. *Environmental Chemistry Letters*, **21**, 55-80. https://doi.org/10.1007/s10311-022-01499-6

[19] Luo, L., Wang, J., Lv, J., Liu, Z., Sun, T., Yang, Y., *et al*. (2023) Carbon Sequestration Strategies in Soil Using Biochar: Advances, Challenges, and Opportunities. *Environmental Science & Technology*, **57**, 11357-11372. https://doi.org/10.1021/acs.est.3c02620

[20] Bessong, M., Bomolomo, M.V., Mbesse, C.O., Mbassa, B.J., Mioumndé, A.P., Hell, J.V., *et al*. (2022) The Garoua Formation of the Upper Benue Trough (Cameroon), as a Potential Lateral Extension of the Bima Formation (Nigeria): Evidence from Geomorphology, Facies Analysis, Petrology and Geochemistry. *Arabian Journal of Geosciences*, **15**, Article No. 915. https://doi.org/10.1007/s12517-022-10078-6

[21] Peña-Monné, J.L., Sampietro-Vattuone, M.M., Báez, W.A., García-Giménez, R., Stábile, F.M., Martínez Stagnaro, S.Y., *et al*. (2021) Sandstone Weathering Processes in the Painted Rock Shelters of Cerro Colorado (Córdoba, Argentina). *Geoarchaeology*, **37**, 332-349. https://doi.org/10.1002/gea.21890

[22] Kobawila, N.D., Elenga, H. and Ngatse, L.R. (2021) Miocene Foraminifera Biostratigraphy and Interpretation North Deep Sea Block of the Congolese Atlantic Basin. *Open Journal of Geology*, **11**, 253-274. https://doi.org/10.4236/ojg.2021.117015

[23] Eshraghi, A. and Zare, S. (2015) Face Stability Evaluation of a TBM-Driven Tunnel in Heterogeneous Soil Using a Probabilistic Approach. *International Journal of Geomechanics*, **15**, Article 04014095. https://doi.org/10.1061/(asce)gm.1943-5622.0000452

[24] Chen, X., Zhang, K. and Wang, W. (2023) Seismic Stability Analysis of Tunnel Faces in Heterogeneous and Anisotropic Soils Using Modified Pseudodynamic Method. *Sustainability*, **15**, Article 11083. https://doi.org/10.3390/su151411083

[25] Nousheen, R., Hashmi, I., Rittschof, D. and Capper, A. (2022) Comprehensive Analysis of Spatial Distribution of Microplastics in Rawal Lake, Pakistan Using Trawl Net and Sieve Sampling Methods. *Chemosphere*, **308**, Article ID: 136111. https://doi.org/10.1016/j.chemosphere.2022.136111

[26] Soinne, H., Keskinen, R., Tähtikarhu, M., Kuva, J. and Hyväluoma, J. (2023) Effects of Organic Carbon and Clay Contents on Structure-Related Properties of Arable Soils with High Clay Content. *European Journal of Soil Science*, **74**, e13424. https://doi.org/10.1111/ejss.13424

[27] Carrasco, J.A., Oestreicher, V., Silva, A.S. and Abellán, G. (2023) Magnetism in Two-Dimensional Layered Double Hydroxides. *Applied Clay Science*, **243**, Article ID: 107073. https://doi.org/10.1016/j.clay.2023.107073

[28] Zakhnini, A., Kulenkampff, J., Sauerzapf, S., Pietrzyk, U. and Lippmann-Pipke, J.

(2013) Monte Carlo Simulations of GeoPET Experiments: 3D Images of Tracer Distributions (^{18}F, ^{124}I and ^{58}Co) in Opalinus Clay, Anhydrite and Quartz. *Computers & Geosciences*, **57**, 183-196. https://doi.org/10.1016/j.cageo.2013.03.023

[29] Dhar, M., Muzenda, T.R., Demeusy, Y., Koutsouradi, A., Jensen, P.A., Labbez, C., *et al*. (2025) Evaluation of Characterization Techniques for Selecting Kaolinitic Clays as Supplementary Cementitious Materials: An Interlaboratory Study. *Journal of the American Ceramic Society*, **108**, e20512. https://doi.org/10.1111/jace.20512

[30] Frederickx, L. (2020) An Advanced Mineralogical Study of the Clay Mineral Fraction of the Boom Clay.

[31] Kang, Y., *et al*. (2024) Detrital and Authigenic Clay Minerals in Shales: A Review on Their Identification and Applications. *Heliyon*, **10**, e39239.

[32] Harvey, C.C. (1995) Kaolin Resources of the United States and Their Industrial Utilization. *In Proceedings of the* 1993 *UN Workshop for Industrial Minerals Development in Asia and the Pacific*, **8**, 252-265.

[33] Pruett, R.J. (2016) Kaolin Deposits and Their Uses: Northern Brazil and Georgia, Usa. *Applied Clay Science*, **131**, 3-13. https://doi.org/10.1016/j.clay.2016.01.048

[34] Buyondo, K.A., Kasedde, H. and Kirabira, J.B. (2022) A Comprehensive Review on Kaolin as Pigment for Paint and Coating: Recent Trends of Chemical-Based Paints, Their Environmental Impacts and Regulation. *Case Studies in Chemical and Environmental Engineering*, **6**, Article ID: 100244. https://doi.org/10.1016/j.cscee.2022.100244

[35] Oyebanjo, O., Ekosse, G. and Odiyo, J. (2020) Physico-Chemical, Mineralogical, and Chemical Characterisation of Cretaceous-Paleogene/Neogene Kaolins within Eastern Dahomey and Niger Delta Basins from Nigeria: Possible Industrial Applications. *Minerals*, **10**, Article No. 670. https://doi.org/10.3390/min10080670

[36] El Hady, A.M.L., Baioumy, H., Dekayir, A., Sabbar, M.S., Abdeina, E.H., El Ghastalany, R., *et al*. (2024) Mineralogy, Geochemistry, Origin, and Potential Industrial Applications of Kaolin Deposit from Hassi Abyad, Mauritania. *Journal of African Earth Sciences*, **214**, Article ID: 105243. https://doi.org/10.1016/j.jafrearsci.2024.105243

[37] Mesele, A., Gidey, T., Weldemaryam, T., Mulualem, W., Mekuria, T., Ali, Y., *et al*. (2021) Mineralogical and Geochemical Characterisation of Kaolin Deposit from Debre Tabor Area Northwestern, Ethiopia. *Applied Earth Science*, **130**, 42-56. https://doi.org/10.1080/25726838.2021.1872820

[38] Bartley, P.C., Fonteno, W.C. and Jackson, B.E. (2022) A Review and Analysis of Horticultural Substrate Characterization by Sieve Analysis. *HortScience*, **57**, 715-725. https://doi.org/10.21273/hortsci16583-22

[39] Manuwa, S.I., Sedara, A.M. and Tola, F.A. (2020) Design, Fabrication and Performance Evaluation of Moringa (Oleifera) Dried Leaves Pulverizer. *Journal of Agriculture and Food Research*, **2**, Article ID: 100034. https://doi.org/10.1016/j.jafr.2020.100034

[40] Stempkowska, A., Gawenda, T., Chajec, A. and Sadowski, Ł. (2022) Effect of Granite Powder Grain Size and Grinding Time of the Properties of Cementitious Composites. *Materials*, **15**, Article No. 8837. https://doi.org/10.3390/ma15248837

[41] Červenka, L., Frühbauerová, M., Palarčík, J., Muriqi, S. and Velichová, H. (2022) The Effect of Vibratory Grinding Time on Moisture Sorption, Particle Size Distribution, and Phenolic Bioaccessibility of Carob Powder. *Molecules*, **27**, Article No. 7689. https://doi.org/10.3390/molecules27227689

[42] Bianchini, M., Wang, J., Clément, R.J., Ouyang, B., Xiao, P., Kitchaev, D., *et al*. (2020)

The Interplay between Thermodynamics and Kinetics in the Solid-State Synthesis of Layered Oxides. *Nature Materials*, **19**, 1088-1095. https://doi.org/10.1038/s41563-020-0688-6

[43] Sahoo, D. and Naik, R. (2022) GSST Phase Change Materials and Its Utilization in Optoelectronic Devices: A Review. *Materials Research Bulletin*, **148**, Article ID: 111679. https://doi.org/10.1016/j.materresbull.2021.111679

[44] Fultz, B. (2020) Phase Transitions in Materials. Cambridge University Press. https://doi.org/10.1017/9781108641449

[45] Vaßen, R., Mack, D.E., Tandler, M., Sohn, Y.J., Sebold, D. and Guillon, O. (2020) Unique Performance of Thermal Barrier Coatings Made of Yttria-Stabilized Zirconia at Extreme Temperatures (> 1500 ˚C). *Journal of the American Ceramic Society*, **104**, 463-471. https://doi.org/10.1111/jace.17452

[46] Song, X., Ding, Y., Zhang, J., Jiang, C., Liu, Z., Lin, C., *et al*. (2023) Thermophysical and Mechanical Properties of Cubic, Tetragonal and Monoclinic ZrO_2. *Journal of Materials Research and Technology*, **23**, 648-655. https://doi.org/10.1016/j.jmrt.2023.01.040

[47] Zhou, D., Mack, D.E., Bakan, E., Mauer, G., Sebold, D., Guillon, O., *et al*. (2019) Thermal Cycling Performances of Multilayered Yttria-stabilized Zirconia/Gadolinium Zirconate Thermal Barrier Coatings. *Journal of the American Ceramic Society*, **103**, 2048-2061. https://doi.org/10.1111/jace.16862

[48] Luo, Q., Fang, X., Liu, L., Yang, C. and Sun, Y. (2020) Automated Visual Defect Detection for Flat Steel Surface: A Survey. *IEEE Transactions on Instrumentation and Measurement*, **69**, 626-644. https://doi.org/10.1109/tim.2019.2963555

[49] Zhang, C., Xue, L., Pestka, S.A., Ranaiefar, M., Atli, K.C., Honarmandi, P., *et al*. (2022) Processing Parameters and Martensitic Phase Transformation Relationships in near Defect-Free Additively Manufactured NiTiHf High Temperature Shape Memory Alloys. *Materials & Design*, **222**, Article ID: 110988. https://doi.org/10.1016/j.matdes.2022.110988

[50] Phuhongsung, P., Zhang, M., Devahastin, S. and Mujumdar, A.S. (2022) Defects in 3D/4D Food Printing and Their Possible Solutions: A Comprehensive Review. *Comprehensive Reviews in Food Science and Food Safety*, **21**, 3455-3479. https://doi.org/10.1111/1541-4337.12984

[51] Dericquebourg, P., Person, A., Ségalen, L., Pickford, M., Senut, B. and Fagel, N. (2019) Bone Diagenesis and Origin of Calcium Phosphate Nodules from a Hominid Site in the Lukeino Formation (Tugen Hills, Kenya). *Palaeogeography, Palaeoclimatology, Palaeoecology*, **536**, Article ID: 109377. https://doi.org/10.1016/j.palaeo.2019.109377

[52] Abdul Rahman, F.S., Abdullah, A.M., Radhi, A., Shahidan, W.N.S. and Abdullah, J.Y. (2023) Physicochemical Characterization of Thermally Processed Goose Bone Ash for Bone Regeneration. *Journal of Functional Biomaterials*, **14**, Article No. 351. https://doi.org/10.3390/jfb14070351

[53] Bih, N.L., Mahamat, A.A., Chinweze, C., Ayeni, O., Bidossèssi, H.J., Onwualu, P.A., *et al*. (2022) The Effect of Bone Ash on the Physio-Chemical and Mechanical Properties of Clay Ceramic Bricks. *Buildings*, **12**, Article No. 336. https://doi.org/10.3390/buildings12030336

[54] Logeshwaran, A., Elsen, R. and Nayak, S. (2023) Mechanical and Biological Characteristics of 3D Fabricated Clay Mineral and Bioceramic Composite Scaffold for Bone Tissue Applications. *Journal of the Mechanical Behavior of Biomedical Materials*, **138**, Article ID: 105633. https://doi.org/10.1016/j.jmbbm.2022.105633

[55] Bhuiya, A.W., Hu, M., Sankar, K., Keane, P.F., Ribero, D. and Kriven, W.M. (2021) Bone Ash Reinforced Geopolymer Composites. *Journal of the American Ceramic Society*, **104**, 2767-2779. https://doi.org/10.1111/jace.17621

[56] Tardio-Brise, L. (2022) Complete Guide to Paper Clay: Mixing Recipes; Building, Finishing and Firing; 10 Practice Projects. Rowman & Littlefield.

[57] Liu, M., *et al*. (2021) Walnut Fruit Processing Equipment: Academic Insights and Perspectives. *Food Engineering Reviews*, **13**, 822-857.

[58] Alneasan, M., Alzo'ubi, A.K., Behnia, M. and Mughieda, O. (2022) Experimental Observations on the Effect of Thermal Treatment on the Crack Speed and Mode I and II Fracture Toughness in Brittle and Ductile Rocks. *Theoretical and Applied Fracture Mechanics*, **121**, Article ID: 103525. https://doi.org/10.1016/j.tafmec.2022.103525

[59] Zhang, Y., Wang, K., Wang, B. and Zhang, C. (2020) Thermal Shock Resistance of Porous Ceramic Foams with Temperature-Dependent Material Properties. *Ceramics International*, **46**, 1503-1511. https://doi.org/10.1016/j.ceramint.2019.09.117

[60] Shu, X., Xu, Y., Li, Y., Yan, W., Wang, Q. and Liang, X. (2023) Preparation of Closed-Pore MgO-$MgFe_2O_4$ Aggregates with Low Thermal Conductivity and High Mechanical Properties. *Journal of the European Ceramic Society*, **43**, 7178-7188. https://doi.org/10.1016/j.jeurceramsoc.2023.06.075

[61] Pakseresht, A., Sharifianjazi, F., Esmaeilkhanian, A., Bazli, L., Reisi Nafchi, M., Bazli, M., *et al*. (2022) Failure Mechanisms and Structure Tailoring of YSZ and New Candidates for Thermal Barrier Coatings: A Systematic Review. *Materials & Design*, **222**, Article ID: 111044. https://doi.org/10.1016/j.matdes.2022.111044

[62] Zhao, H., Ma, Y., Zhang, J., Hu, Z., Li, H., Wang, Y., *et al*. (2022) Effect of Clay Content on Shrinkage of Cementitious Materials. *Construction and Building Materials*, **322**, Article ID: 125959. https://doi.org/10.1016/j.conbuildmat.2021.125959

[63] Pokharel, B. and Siddiqua, S. (2021) Understanding the Effect of Pulp Mill Fly Ash on Strength, Compressibility, and Microstructure of Organic Soil. *International Journal of Geomechanics*, **21**, Article ID: 04021209. https://doi.org/10.1061/(asce)gm.1943-5622.0002172

[64] Ko, E., Lim, D., Kim, S., Youk, J. and Jeon, H. (2023) Bending Strength Evaluation of Three-Dimensional Double Rachel Geosynthetic Cementitious Composite Mat (GCCM) under Environmental Conditions. *Applied Sciences*, **13**, Article No. 11271. https://doi.org/10.3390/app132011271

[65] Zhang, Z., Zhao, Y. and Liu, K. (2024) The Effect of High-Energy Ball Milling on Enhancing the Mechanical Properties, Light Transmittance, and Thermal Shock Resistance of Bone China Porcelain. *Ceramics International*, **50**, 53552-53561. https://doi.org/10.1016/j.ceramint.2024.10.204

[66] Ibrahim, J.E.F.M., Tihtih, M., Kurovics, E., Gömze, L.A. and Kocserha, I. (2022) Innovative Glass-Ceramic Foams Prepared by Alkali Activation and Reactive Sintering of Clay Containing Zeolite (Zeolite-Poor Rock) and Sawdust for Thermal Insulation. *Journal of Building Engineering*, **59**, Article ID: 105160. https://doi.org/10.1016/j.jobe.2022.105160

[67] Li, F., Yin, D., Zhu, C., Wang, F., Jiang, N. and Zhang, Z. (2021) Effects of Kaolin Addition on Mechanical Properties for Cemented Coal Gangue-Fly Ash Backfill under Uniaxial Loading. *Energies*, **14**, Article No. 3693. https://doi.org/10.3390/en14123693

[68] Hill, C., Altgen, M. and Rautkari, L. (2021) Thermal Modification of Wood—A Review: Chemical Changes and Hygroscopicity. *Journal of Materials Science*, **56**, 6581-

6614. https://doi.org/10.1007/s10853-020-05722-z

[69] Singla, M. and Sit, N. (2021) Application of Ultrasound in Combination with Other Technologies in Food Processing: A Review. *Ultrasonics Sonochemistry*, **73**, Article ID: 105506. https://doi.org/10.1016/j.ultsonch.2021.105506

[70] Li, X., Lin, Y., Liu, M., Meng, L. and Li, C. (2022) A Review of Research and Application of Polylactic Acid Composites. *Journal of Applied Polymer Science*, **140**, e53477. https://doi.org/10.1002/app.53477

[71] Wang, W., Liu, H., Deng, R. and Wang, Y. (2023) Active Stability Analysis of 3D Tunnel Face in Nonhomogeneous and Anisotropic Soils. *Geotechnical and Geological Engineering*, **41**, 3013-3033. https://doi.org/10.1007/s10706-023-02442-4

[72] Alexander Tangwa, N., Oliver Anoh, N. and Yinkfu Njamnsi, N. (2022) Geotechnical Properties and Geochemical Composition of Mudrock from the Douala Sub Basin, Cameroon: Implication for Industrial Potentials. *Journal of Geosciences and Geomatics*, **10**, 162-171. https://doi.org/10.12691/jgg-10-3-5

[73] Oumar, K.O., Gilbert François, N.N., Bertrand, M.M., Nathanael, T., Constantin, B.E., Simon, M.J., *et al*. (2022) Mineralogical, Geochemical Characterization and Physicochemical Properties of Kaolinitic Clays of the Eastern Part of the Douala Sub-Basin, Cameroon, Central Africa. *Applied Sciences*, **12**, Article No. 9143. https://doi.org/10.3390/app12189143

Appendice

A-stress-strain curves of Bone Ash Clay (BAC-SP) specimens of combinations C1 to C10.

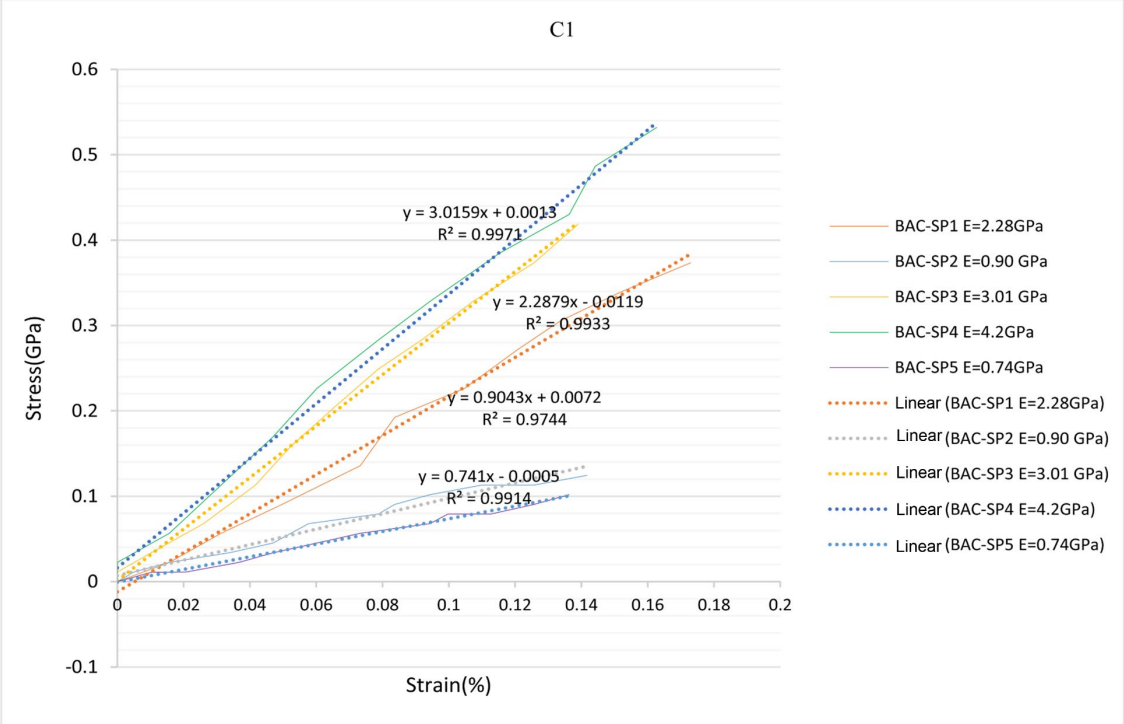

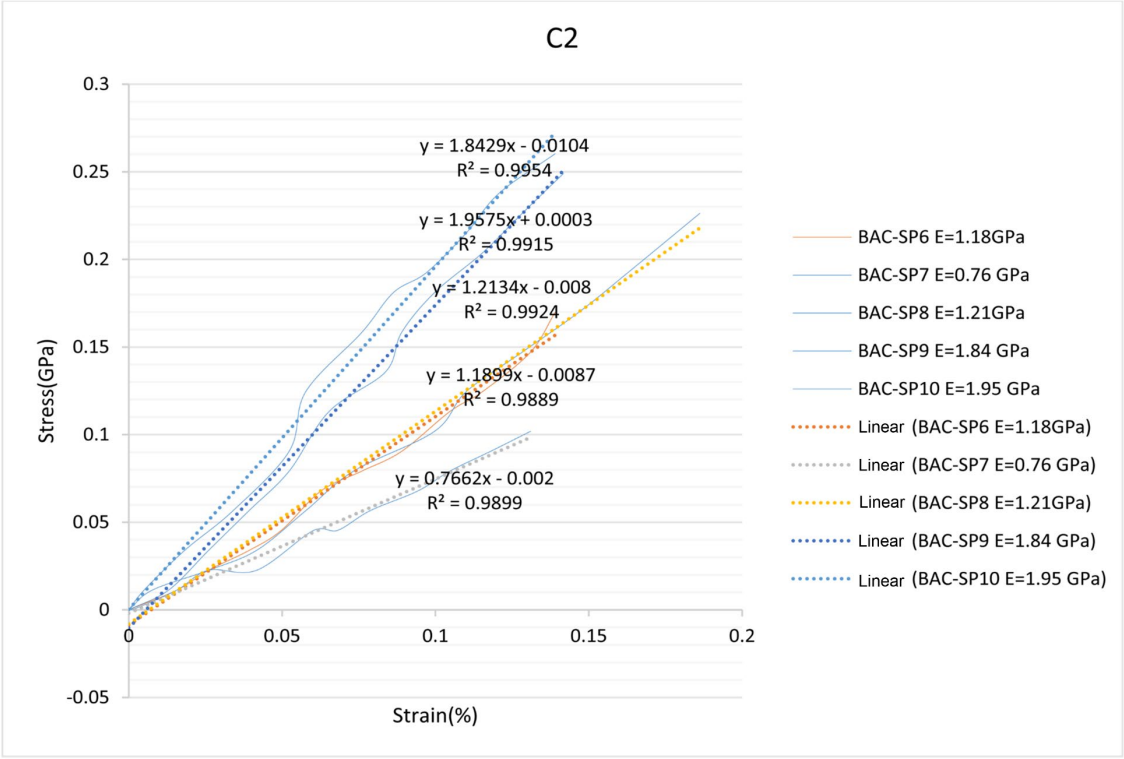

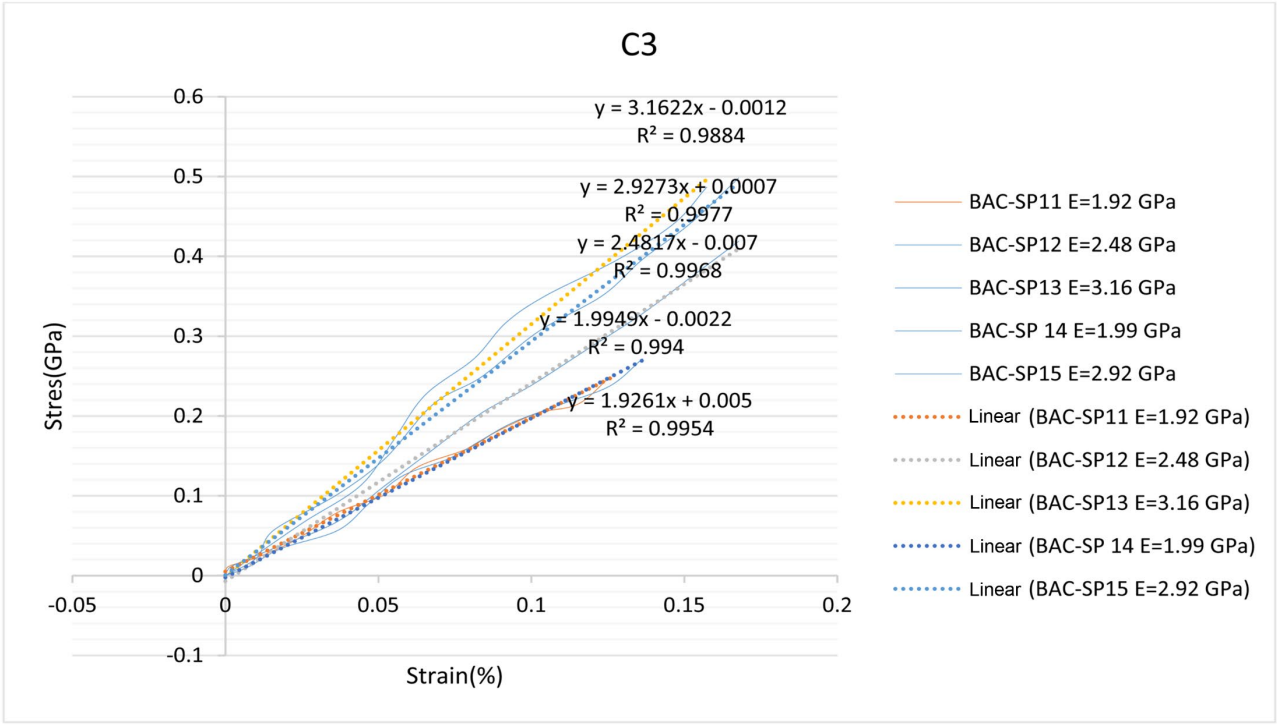
C3
y = 3.1622x - 0.0012
R² = 0.9884
y = 2.9273x + 0.0007
R² = 0.9977
y = 2.4817x - 0.007
R² = 0.9968
y = 1.9949x - 0.0022
R² = 0.994
y = 1.9261x + 0.005
R² = 0.9954
Stres(GPa)
Strain(%)
BAC-SP11 E=1.92 GPa
BAC-SP12 E=2.48 GPa
BAC-SP13 E=3.16 GPa
BAC-SP 14 E=1.99 GPa
BAC-SP15 E=2.92 GPa
Linear (BAC-SP11 E=1.92 GPa)
Linear (BAC-SP12 E=2.48 GPa)
Linear (BAC-SP13 E=3.16 GPa)
Linear (BAC-SP 14 E=1.99 GPa)
Linear (BAC-SP15 E=2.92 GPa)

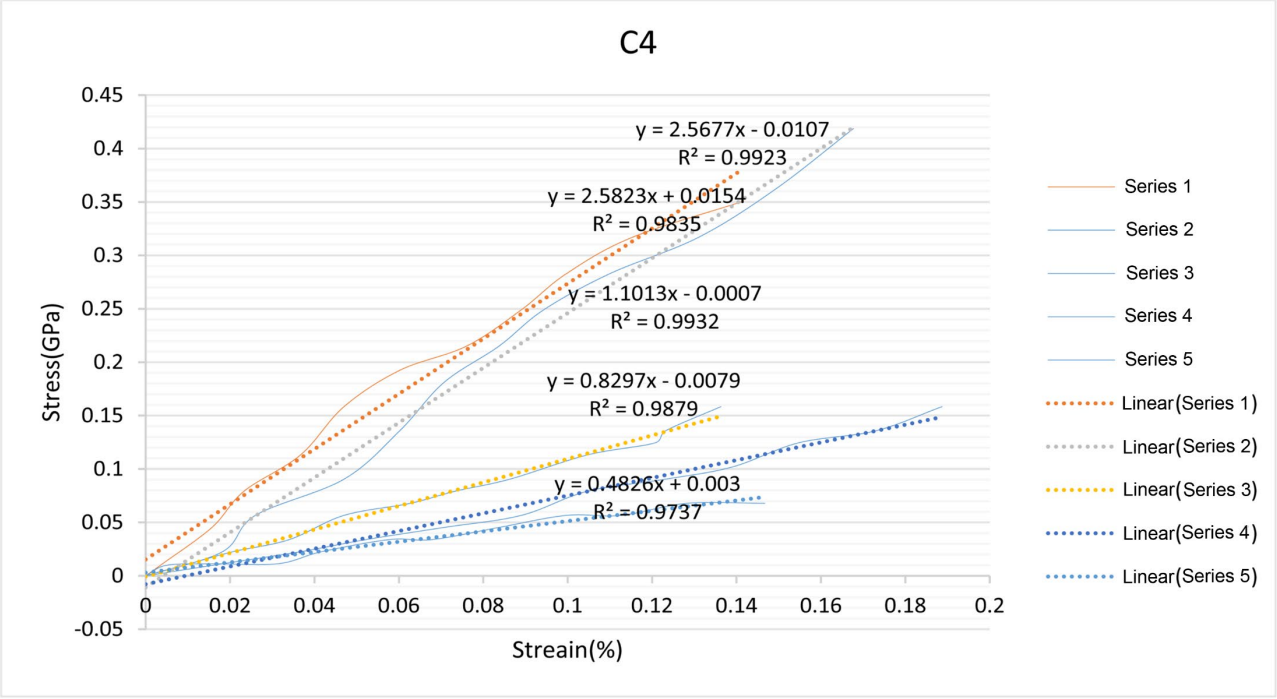
C4
y = 2.5677x - 0.0107
R² = 0.9923
y = 2.5823x + 0.0154
R² = 0.9835
y = 1.1013x - 0.0007
R² = 0.9932
y = 0.8297x - 0.0079
R² = 0.9879
y = 0.4826x + 0.003
R² = 0.9737
Stress(GPa)
Streain(%)
Series 1
Series 2
Series 3
Series 4
Series 5
Linear(Series 1)
Linear(Series 2)
Linear(Series 3)
Linear(Series 4)
Linear(Series 5)

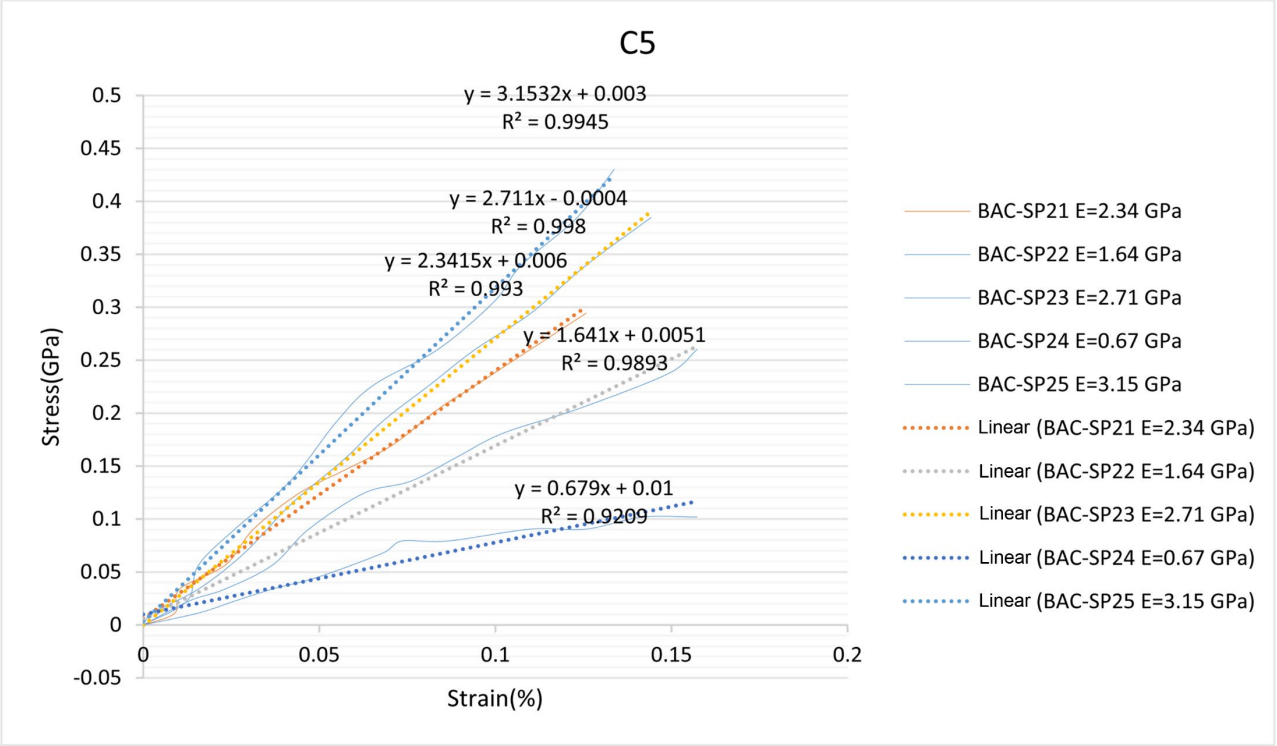
C5
y = 3.1532x + 0.003
R² = 0.9945
y = 2.711x - 0.0004
R² = 0.998
y = 2.3415x + 0.006
R² = 0.993
y = 1.641x + 0.0051
R² = 0.9893
y = 0.679x + 0.01
R² = 0.9209
Stress(GPa)
Strain(%)
BAC-SP21 E=2.34 GPa
BAC-SP22 E=1.64 GPa
BAC-SP23 E=2.71 GPa
BAC-SP24 E=0.67 GPa
BAC-SP25 E=3.15 GPa
Linear (BAC-SP21 E=2.34 GPa)
Linear (BAC-SP22 E=1.64 GPa)
Linear (BAC-SP23 E=2.71 GPa)
Linear (BAC-SP24 E=0.67 GPa)
Linear (BAC-SP25 E=3.15 GPa)

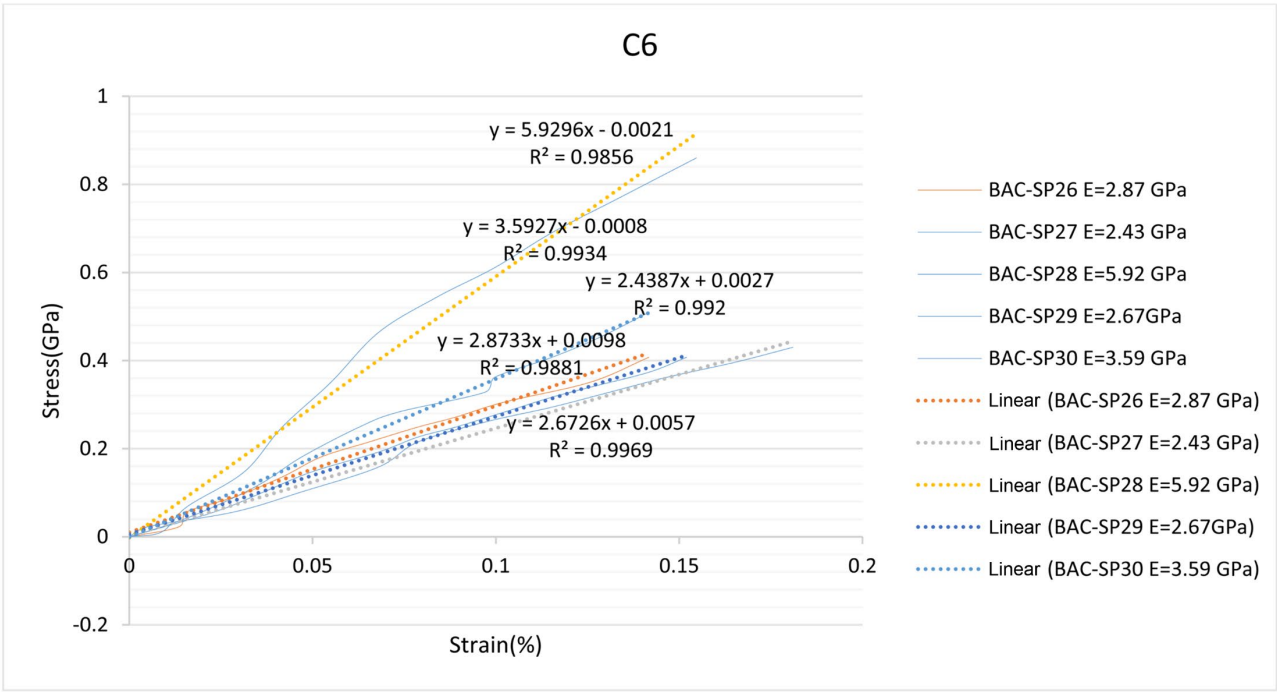
C6
y = 5.9296x - 0.0021
R² = 0.9856
y = 3.5927x - 0.0008
R² = 0.9934
y = 2.4387x + 0.0027
R² = 0.992
y = 2.8733x + 0.0098
R² = 0.9881
y = 2.6726x + 0.0057
R² = 0.9969
Stress(GPa)
Strain(%)
BAC-SP26 E=2.87 GPa
BAC-SP27 E=2.43 GPa
BAC-SP28 E=5.92 GPa
BAC-SP29 E=2.67GPa
BAC-SP30 E=3.59 GPa
Linear (BAC-SP26 E=2.87 GPa)
Linear (BAC-SP27 E=2.43 GPa)
Linear (BAC-SP28 E=5.92 GPa)
Linear (BAC-SP29 E=2.67GPa)
Linear (BAC-SP30 E=3.59 GPa)

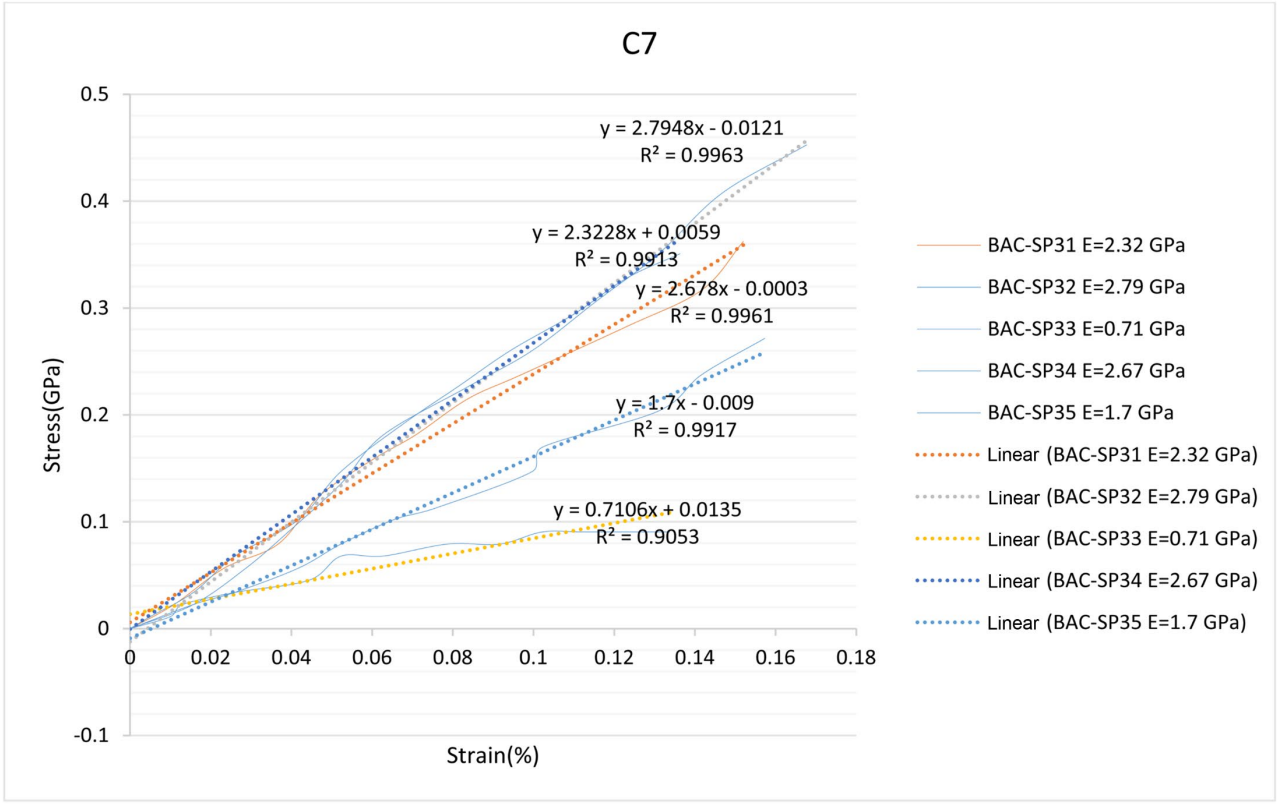
C7
y = 2.7948x - 0.0121
R² = 0.9963
y = 2.3228x + 0.0059
R² = 0.9913
y = 2.678x - 0.0003
R² = 0.9961
y = 1.7x - 0.009
R² = 0.9917
y = 0.7106x + 0.0135
R² = 0.9053
Stress(GPa)
Strain(%)
BAC-SP31 E=2.32 GPa
BAC-SP32 E=2.79 GPa
BAC-SP33 E=0.71 GPa
BAC-SP34 E=2.67 GPa
BAC-SP35 E=1.7 GPa
Linear (BAC-SP31 E=2.32 GPa)
Linear (BAC-SP32 E=2.79 GPa)
Linear (BAC-SP33 E=0.71 GPa)
Linear (BAC-SP34 E=2.67 GPa)
Linear (BAC-SP35 E=1.7 GPa)

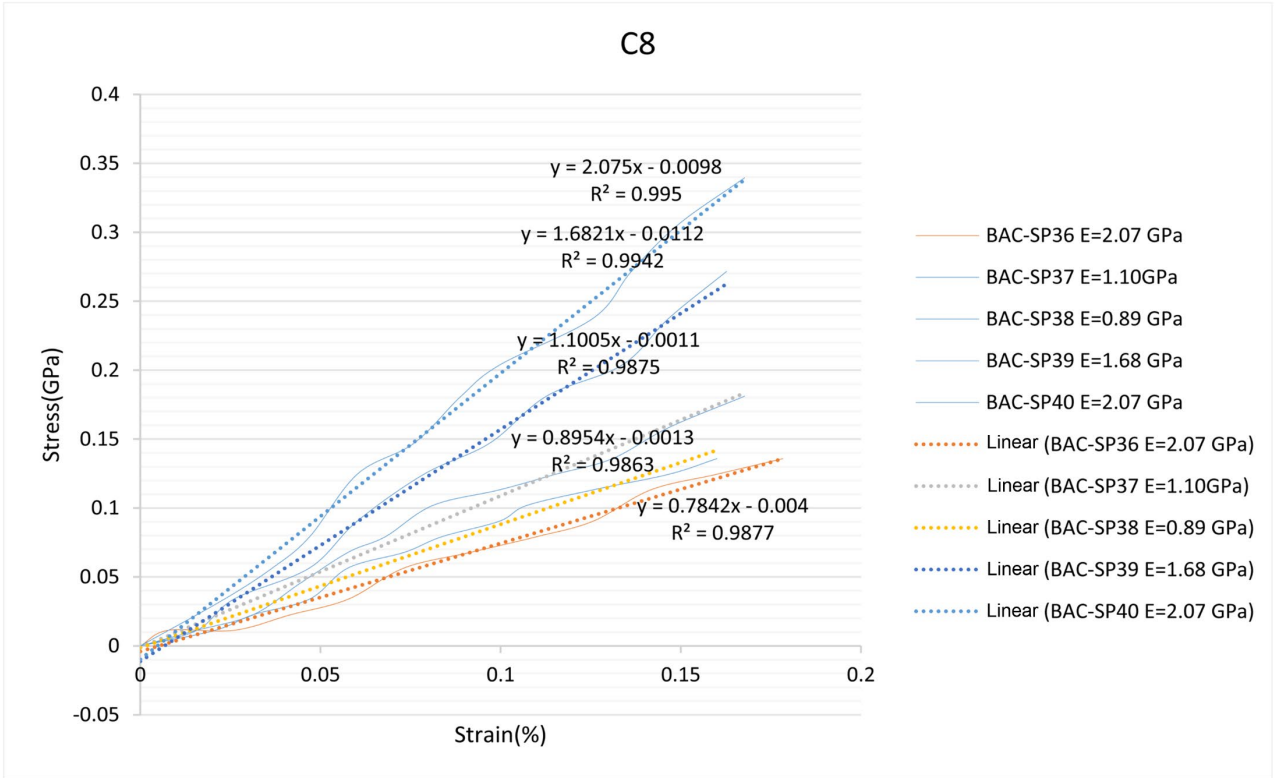
C8
y = 2.075x - 0.0098
R² = 0.995
y = 1.6821x - 0.0112
R² = 0.9942
y = 1.1005x - 0.0011
R² = 0.9875
y = 0.8954x - 0.0013
R² = 0.9863
y = 0.7842x - 0.004
R² = 0.9877
Stress(GPa)
Strain(%)
BAC-SP36 E=2.07 GPa
BAC-SP37 E=1.10GPa
BAC-SP38 E=0.89 GPa
BAC-SP39 E=1.68 GPa
BAC-SP40 E=2.07 GPa
Linear (BAC-SP36 E=2.07 GPa)
Linear (BAC-SP37 E=1.10GPa)
Linear (BAC-SP38 E=0.89 GPa)
Linear (BAC-SP39 E=1.68 GPa)
Linear (BAC-SP40 E=2.07 GPa)

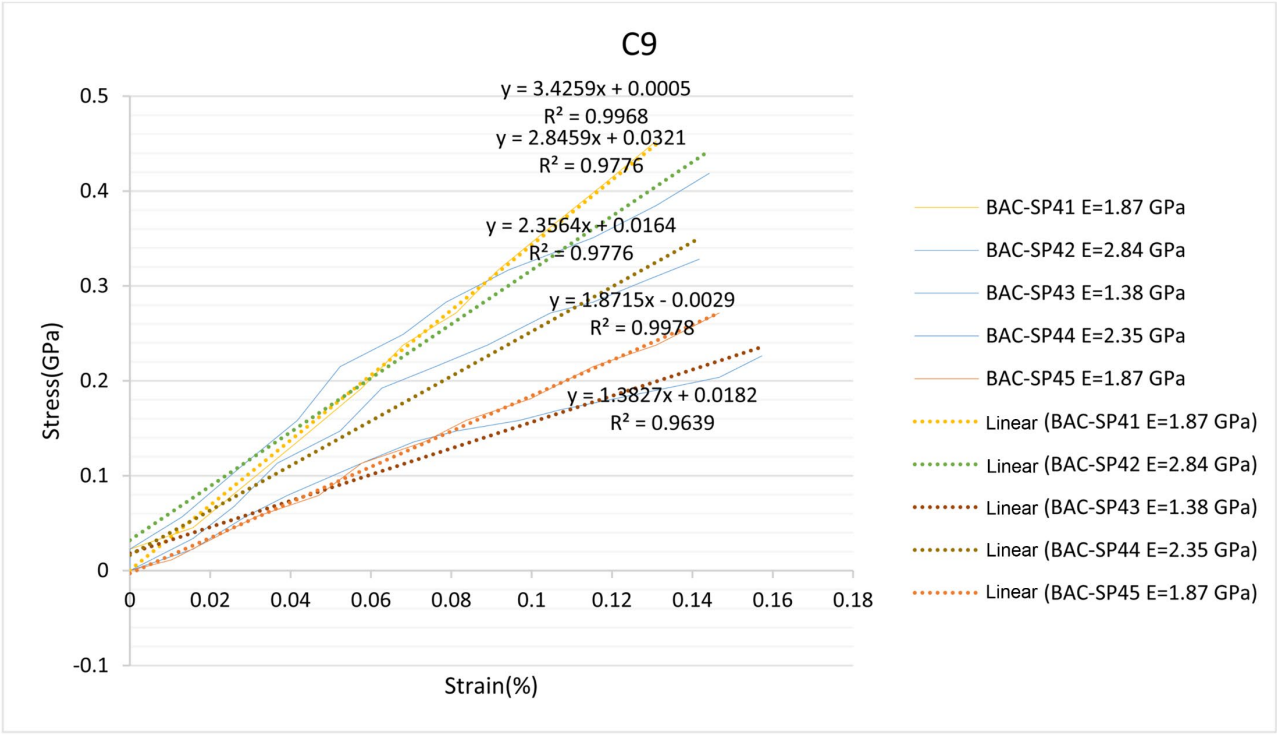
C9
y = 3.4259x + 0.0005
R² = 0.9968
y = 2.8459x + 0.0321
R² = 0.9776
y = 2.3564x + 0.0164
R² = 0.9776
y = 1.8715x - 0.0029
R² = 0.9978
y = 1.3827x + 0.0182
R² = 0.9639
Stress(GPa)
Strain(%)
BAC-SP41 E=1.87 GPa
BAC-SP42 E=2.84 GPa
BAC-SP43 E=1.38 GPa
BAC-SP44 E=2.35 GPa
BAC-SP45 E=1.87 GPa
Linear (BAC-SP41 E=1.87 GPa)
Linear (BAC-SP42 E=2.84 GPa)
Linear (BAC-SP43 E=1.38 GPa)
Linear (BAC-SP44 E=2.35 GPa)
Linear (BAC-SP45 E=1.87 GPa)

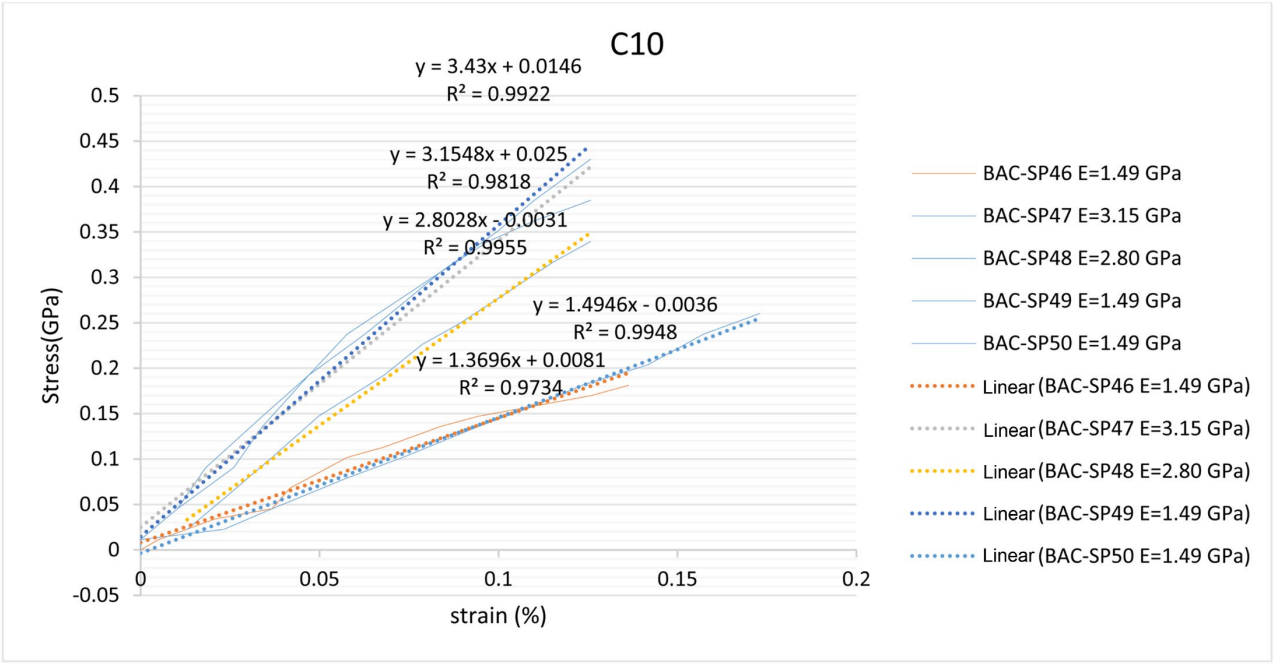
C10
y = 3.43x + 0.0146
R² = 0.9922
y = 3.1548x + 0.025
R² = 0.9818
y = 2.8028x - 0.0031
R² = 0.9955
y = 1.4946x - 0.0036
R² = 0.9948
y = 1.3696x + 0.0081
R² = 0.9734
Stress(GPa)
strain (%)
BAC-SP46 E=1.49 GPa
BAC-SP47 E=3.15 GPa
BAC-SP48 E=2.80 GPa
BAC-SP49 E=1.49 GPa
BAC-SP50 E=1.49 GPa
Linear (BAC-SP46 E=1.49 GPa)
Linear (BAC-SP47 E=3.15 GPa)
Linear (BAC-SP48 E=2.80 GPa)
Linear (BAC-SP49 E=1.49 GPa)
Linear (BAC-SP50 E=1.49 GPa)

B-Stress-strain curves of cylindrical pure clay specimens (CPC-SP) of combinations C1 to C10.

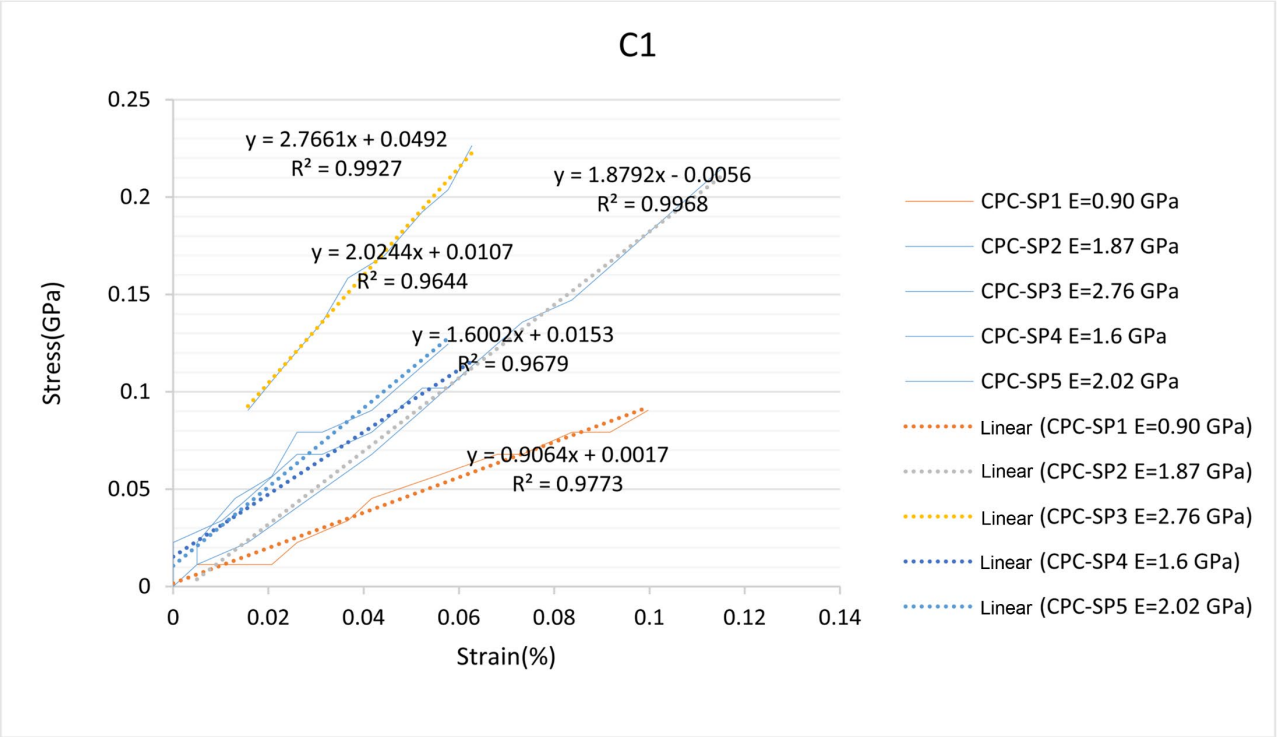

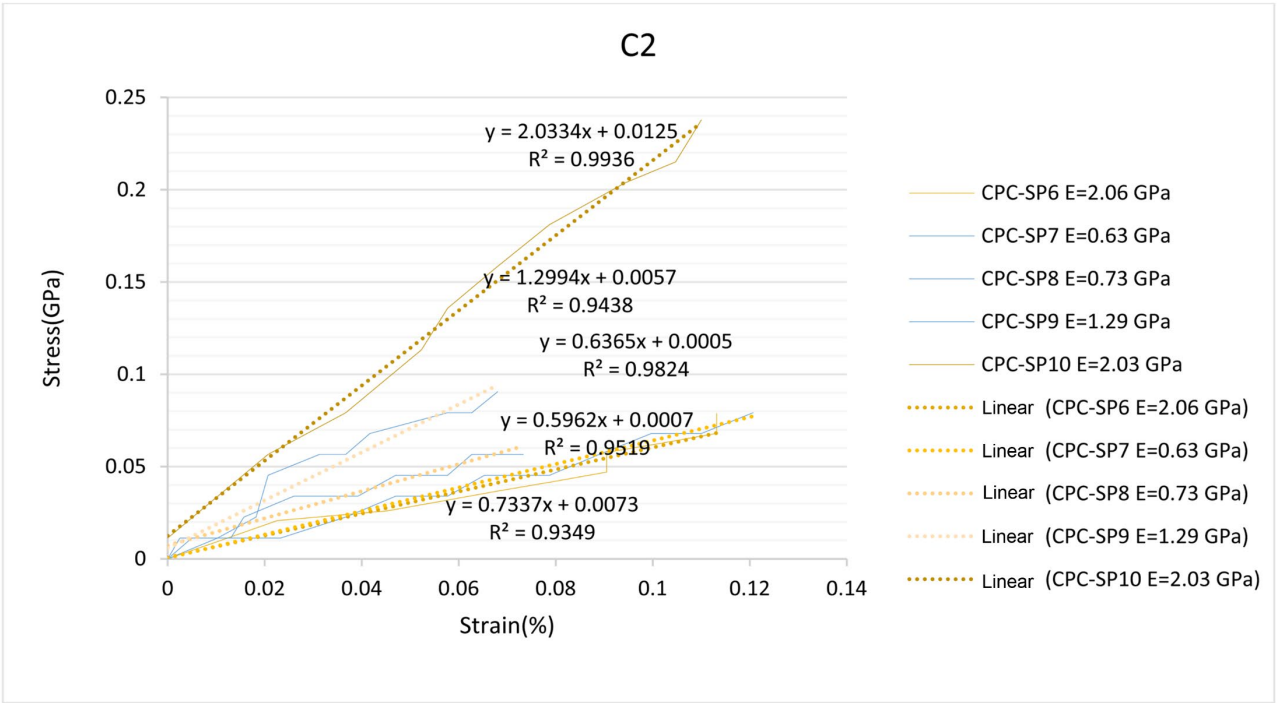

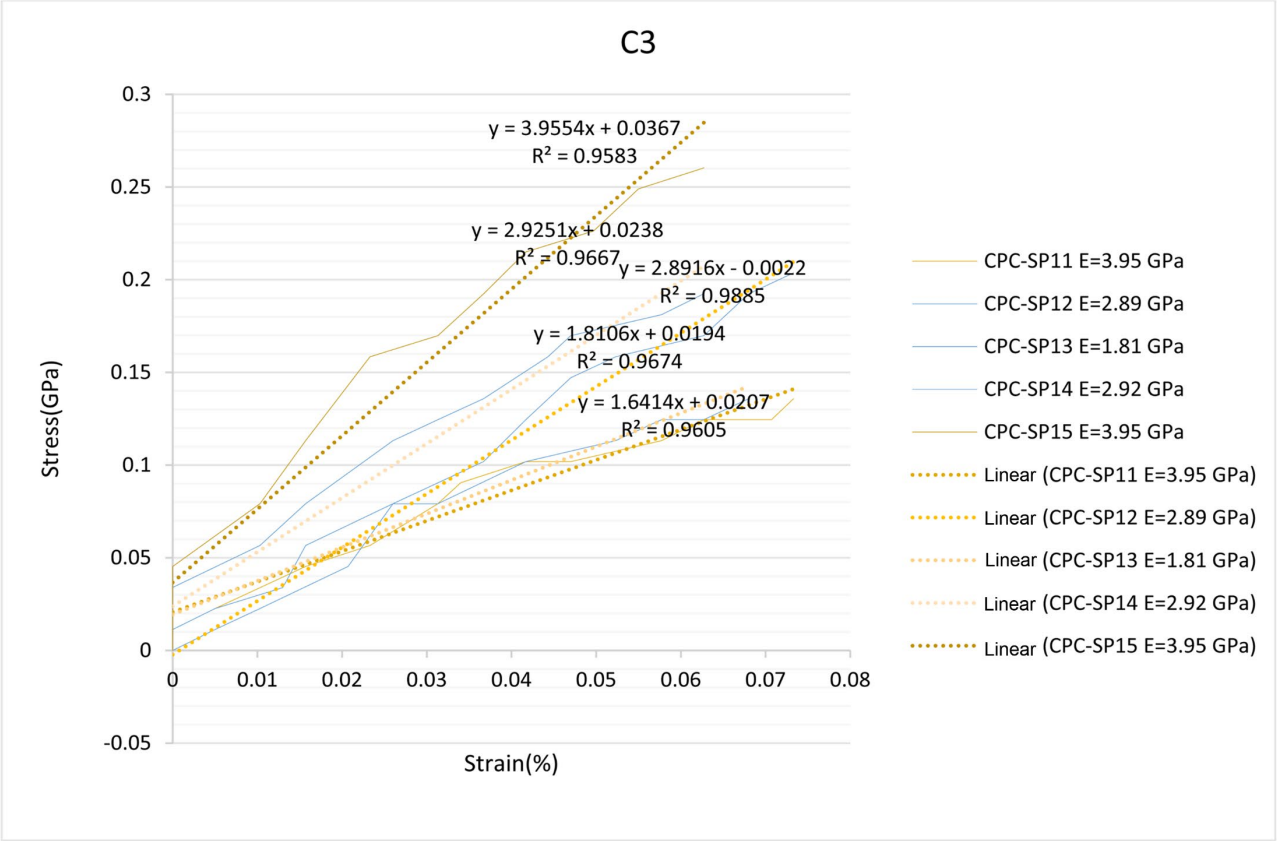
C3
y = 3.9554x + 0.0367
R² = 0.9583
y = 2.9251x + 0.0238
R² = 0.9667
y = 2.8916x - 0.0022
R² = 0.9885
y = 1.8106x + 0.0194
R² = 0.9674
y = 1.6414x + 0.0207
R² = 0.9605
Stress(GPa)
Strain(%)
CPC-SP11 E=3.95 GPa
CPC-SP12 E=2.89 GPa
CPC-SP13 E=1.81 GPa
CPC-SP14 E=2.92 GPa
CPC-SP15 E=3.95 GPa
Linear (CPC-SP11 E=3.95 GPa)
Linear (CPC-SP12 E=2.89 GPa)
Linear (CPC-SP13 E=1.81 GPa)
Linear (CPC-SP14 E=2.92 GPa)
Linear (CPC-SP15 E=3.95 GPa)

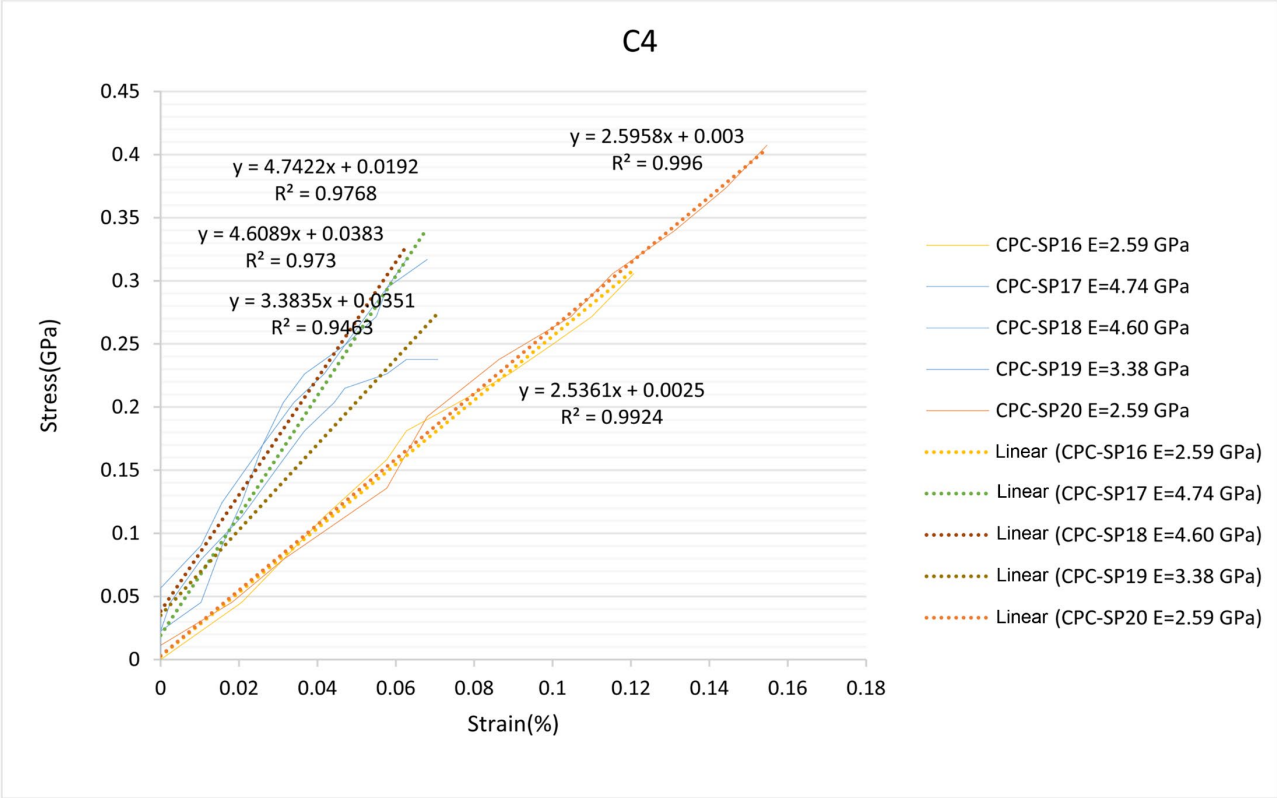
C4
y = 4.7422x + 0.0192
R² = 0.9768
y = 4.6089x + 0.0383
R² = 0.973
y = 3.3835x + 0.0351
R² = 0.9463
y = 2.5958x + 0.003
R² = 0.996
y = 2.5361x + 0.0025
R² = 0.9924
Stress(GPa)
Strain(%)
CPC-SP16 E=2.59 GPa
CPC-SP17 E=4.74 GPa
CPC-SP18 E=4.60 GPa
CPC-SP19 E=3.38 GPa
CPC-SP20 E=2.59 GPa
Linear (CPC-SP16 E=2.59 GPa)
Linear (CPC-SP17 E=4.74 GPa)
Linear (CPC-SP18 E=4.60 GPa)
Linear (CPC-SP19 E=3.38 GPa)
Linear (CPC-SP20 E=2.59 GPa)

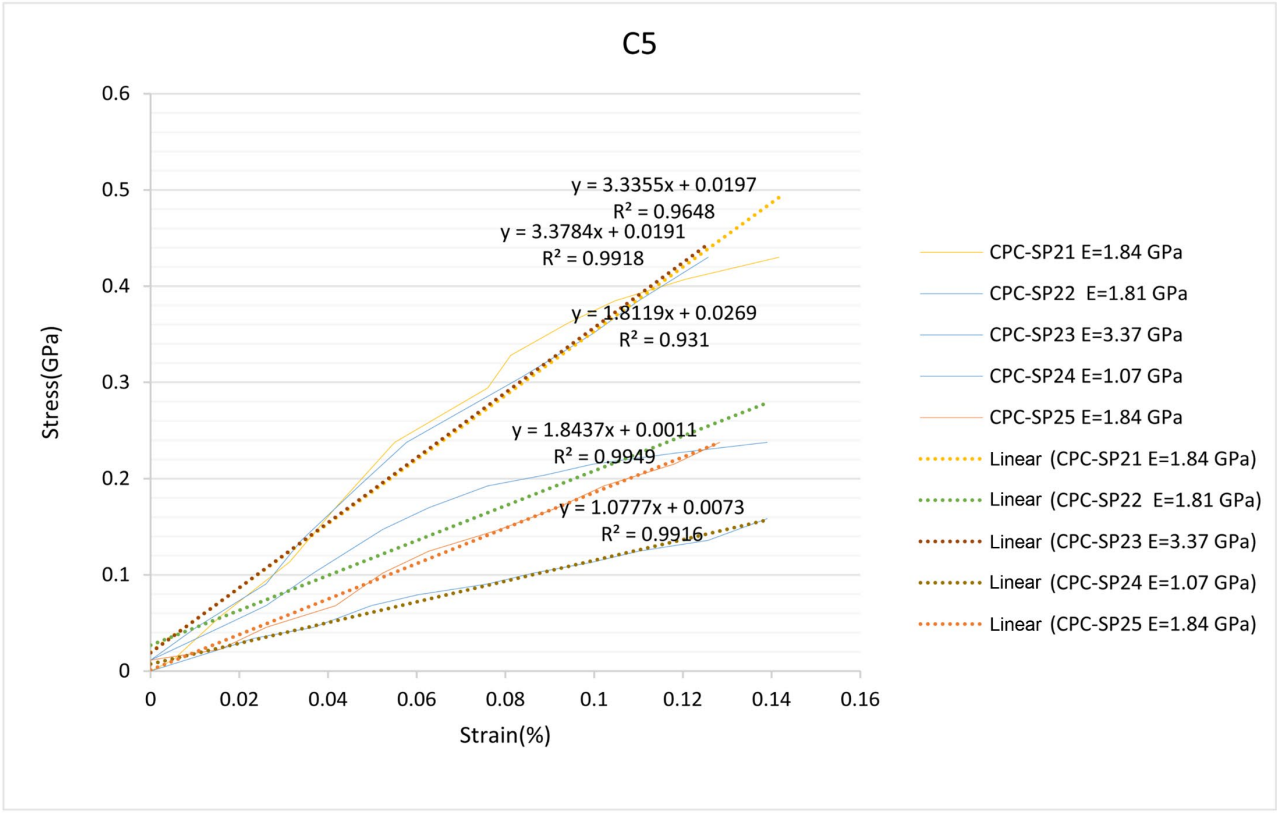
C5
Stress(GPa)
Strain(%)
y = 3.3355x + 0.0197
R² = 0.9648
y = 3.3784x + 0.0191
R² = 0.9918
y = 1.8119x + 0.0269
R² = 0.931
y = 1.8437x + 0.0011
R² = 0.9949
y = 1.0777x + 0.0073
R² = 0.9916
CPC-SP21 E=1.84 GPa
CPC-SP22 E=1.81 GPa
CPC-SP23 E=3.37 GPa
CPC-SP24 E=1.07 GPa
CPC-SP25 E=1.84 GPa
Linear (CPC-SP21 E=1.84 GPa)
Linear (CPC-SP22 E=1.81 GPa)
Linear (CPC-SP23 E=3.37 GPa)
Linear (CPC-SP24 E=1.07 GPa)
Linear (CPC-SP25 E=1.84 GPa)

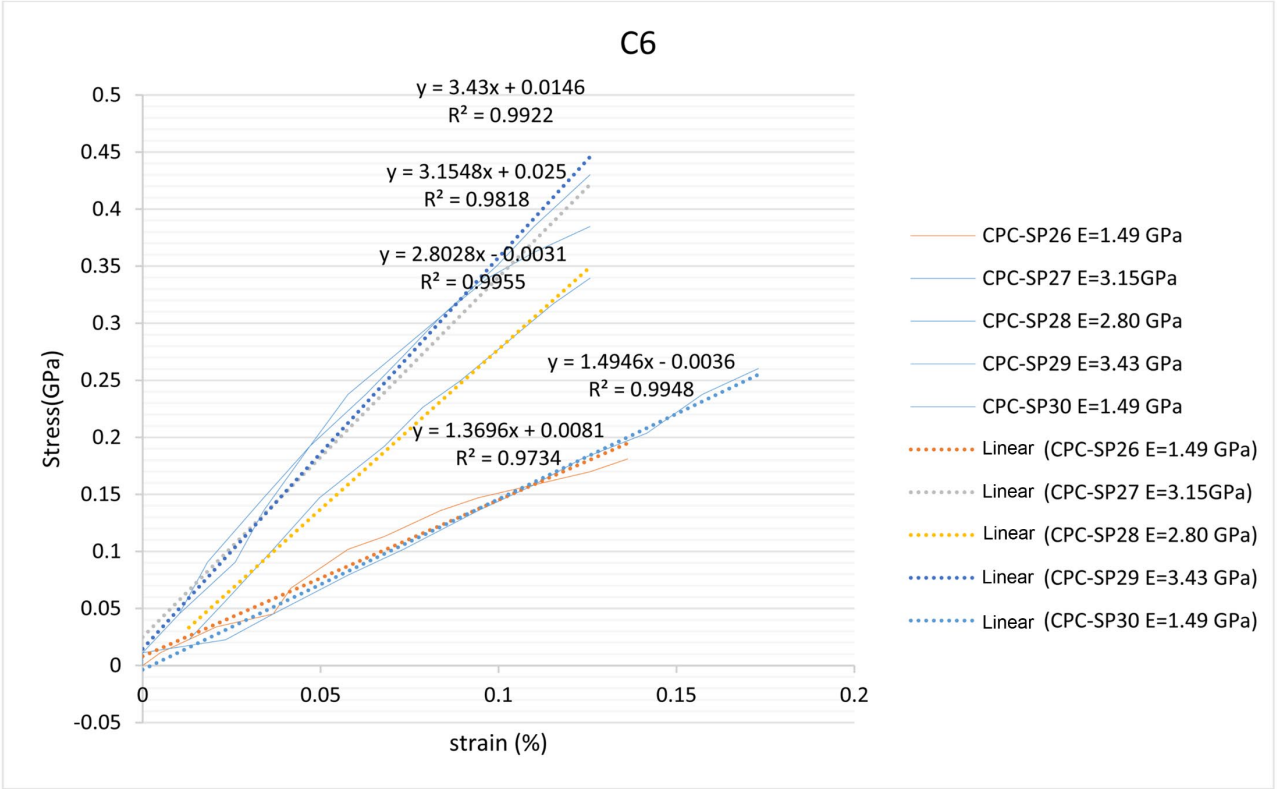
C6
Stress(GPa)
strain (%)
y = 3.43x + 0.0146
R² = 0.9922
y = 3.1548x + 0.025
R² = 0.9818
y = 2.8028x - 0.0031
R² = 0.9955
y = 1.4946x - 0.0036
R² = 0.9948
y = 1.3696x + 0.0081
R² = 0.9734
CPC-SP26 E=1.49 GPa
CPC-SP27 E=3.15GPa
CPC-SP28 E=2.80 GPa
CPC-SP29 E=3.43 GPa
CPC-SP30 E=1.49 GPa
Linear (CPC-SP26 E=1.49 GPa)
Linear (CPC-SP27 E=3.15GPa)
Linear (CPC-SP28 E=2.80 GPa)
Linear (CPC-SP29 E=3.43 GPa)
Linear (CPC-SP30 E=1.49 GPa)

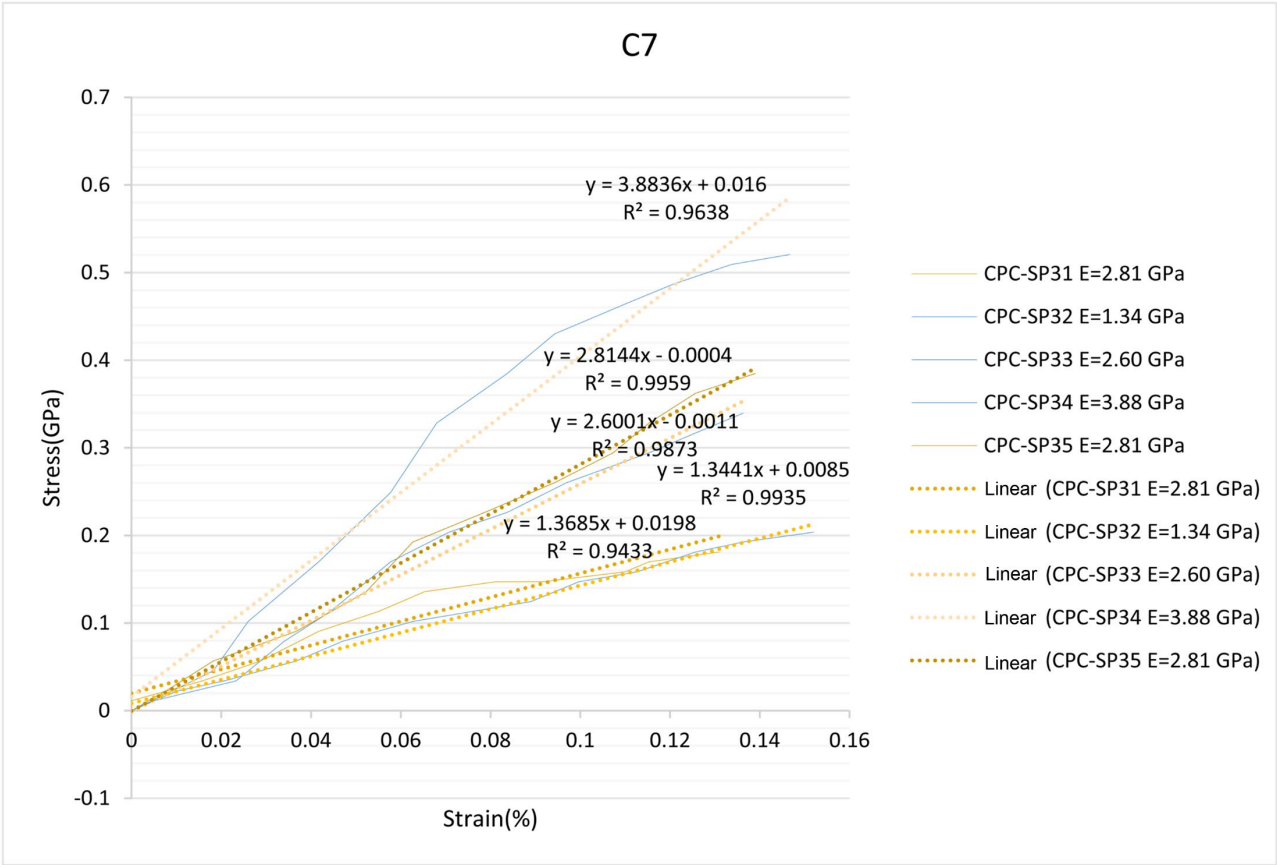
C7
y = 3.8836x + 0.016
R² = 0.9638
y = 2.8144x - 0.0004
R² = 0.9959
y = 2.6001x - 0.0011
R² = 0.9873
y = 1.3441x + 0.0085
R² = 0.9935
y = 1.3685x + 0.0198
R² = 0.9433
Stress(GPa)
Strain(%)
CPC-SP31 E=2.81 GPa
CPC-SP32 E=1.34 GPa
CPC-SP33 E=2.60 GPa
CPC-SP34 E=3.88 GPa
CPC-SP35 E=2.81 GPa
Linear (CPC-SP31 E=2.81 GPa)
Linear (CPC-SP32 E=1.34 GPa)
Linear (CPC-SP33 E=2.60 GPa)
Linear (CPC-SP34 E=3.88 GPa)
Linear (CPC-SP35 E=2.81 GPa)

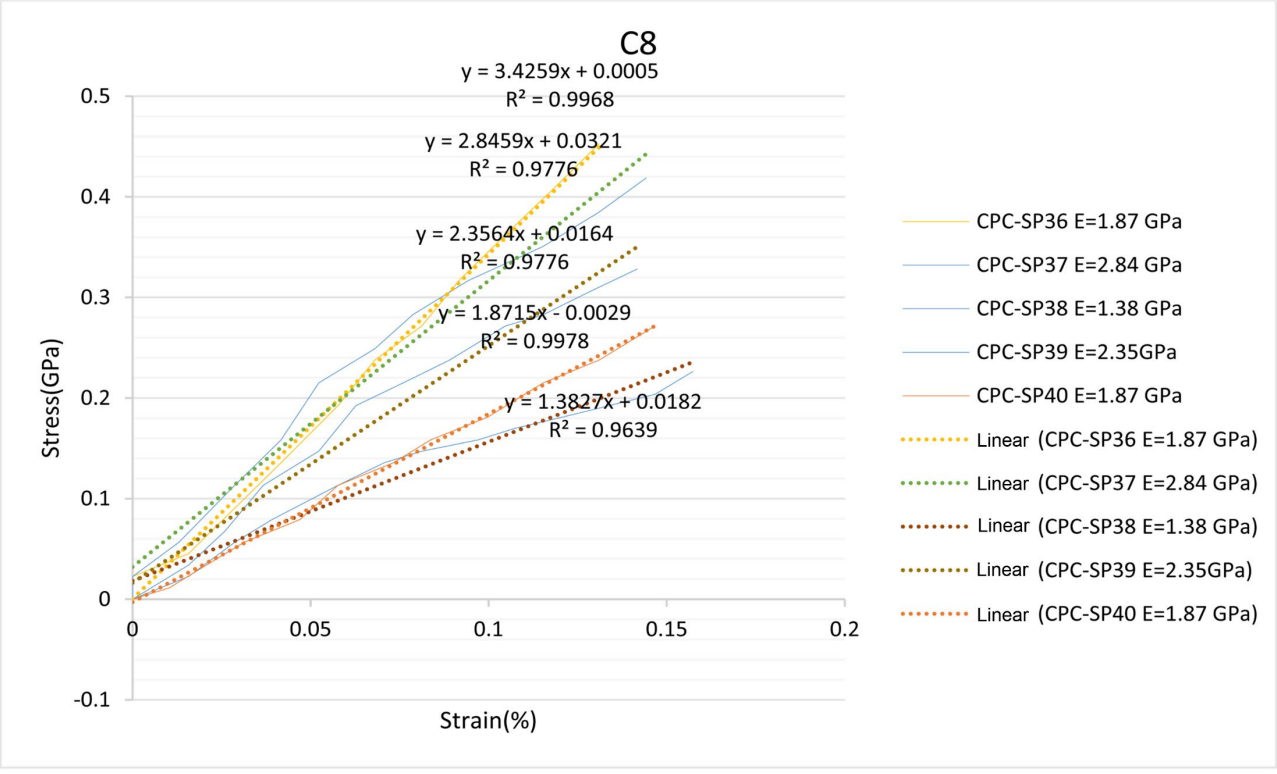
C8
y = 3.4259x + 0.0005
R² = 0.9968
y = 2.8459x + 0.0321
R² = 0.9776
y = 2.3564x + 0.0164
R² = 0.9776
y = 1.8715x - 0.0029
R² = 0.9978
y = 1.3827x + 0.0182
R² = 0.9639
Stress(GPa)
Strain(%)
CPC-SP36 E=1.87 GPa
CPC-SP37 E=2.84 GPa
CPC-SP38 E=1.38 GPa
CPC-SP39 E=2.35GPa
CPC-SP40 E=1.87 GPa
Linear (CPC-SP36 E=1.87 GPa)
Linear (CPC-SP37 E=2.84 GPa)
Linear (CPC-SP38 E=1.38 GPa)
Linear (CPC-SP39 E=2.35GPa)
Linear (CPC-SP40 E=1.87 GPa)

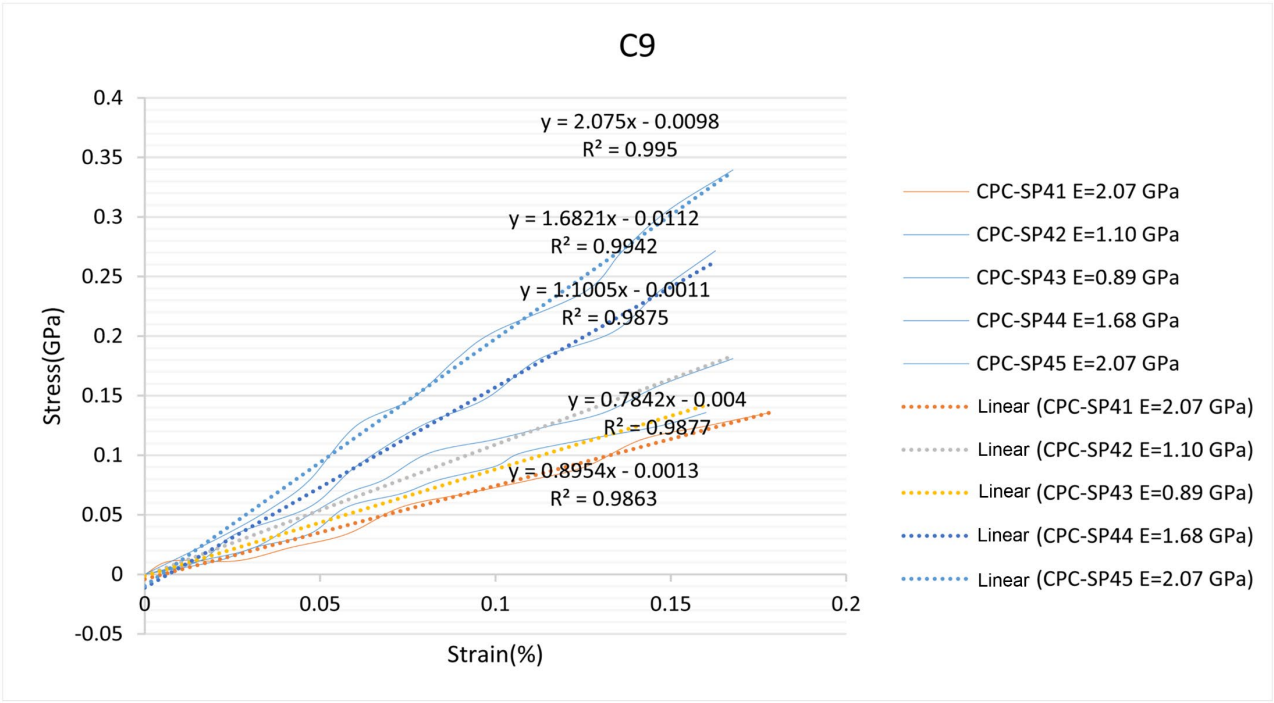
C9
y = 2.075x - 0.0098
R² = 0.995
y = 1.6821x - 0.0112
R² = 0.9942
y = 1.1005x - 0.0011
R² = 0.9875
y = 0.7842x - 0.004
R² = 0.9877
y = 0.8954x - 0.0013
R² = 0.9863
Stress(GPa)
Strain(%)
CPC-SP41 E=2.07 GPa
CPC-SP42 E=1.10 GPa
CPC-SP43 E=0.89 GPa
CPC-SP44 E=1.68 GPa
CPC-SP45 E=2.07 GPa
Linear (CPC-SP41 E=2.07 GPa)
Linear (CPC-SP42 E=1.10 GPa)
Linear (CPC-SP43 E=0.89 GPa)
Linear (CPC-SP44 E=1.68 GPa)
Linear (CPC-SP45 E=2.07 GPa)

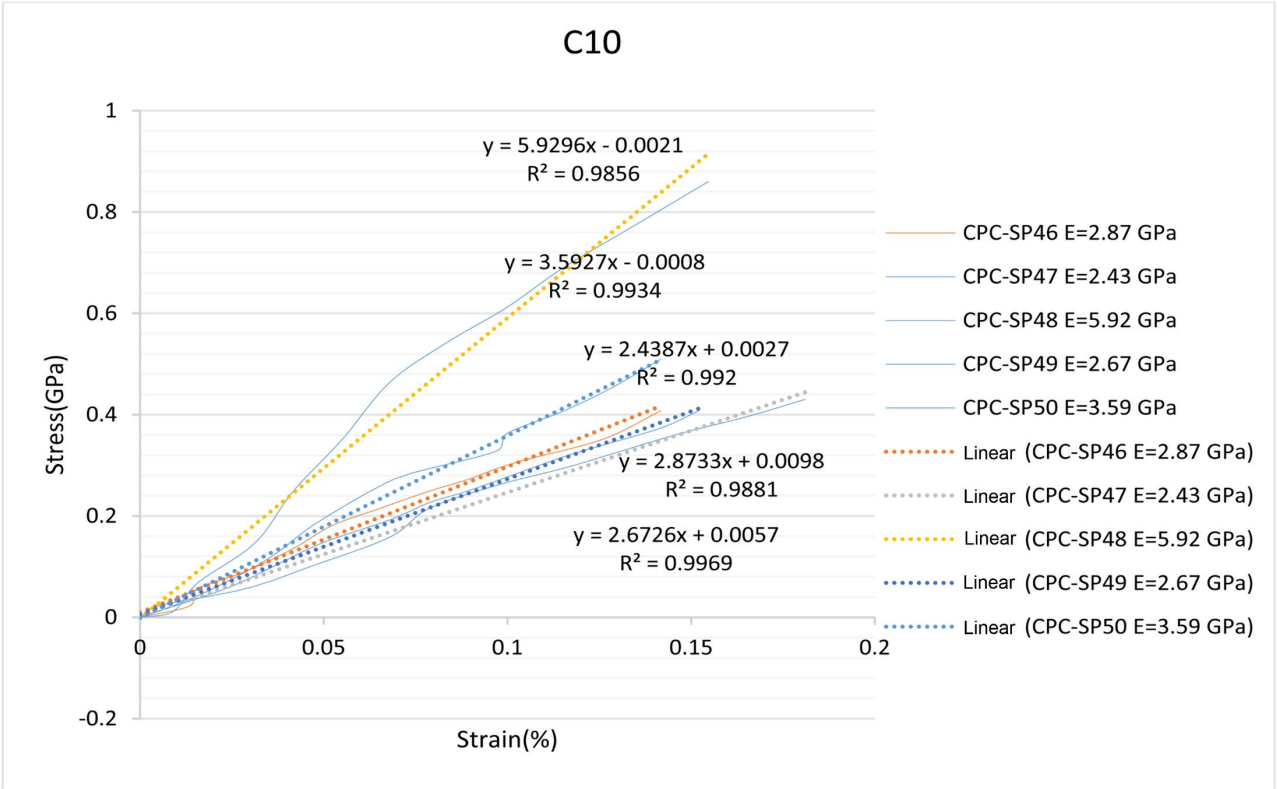
C10
y = 5.9296x - 0.0021
R² = 0.9856
y = 3.5927x - 0.0008
R² = 0.9934
y = 2.4387x + 0.0027
R² = 0.992
y = 2.8733x + 0.0098
R² = 0.9881
y = 2.6726x + 0.0057
R² = 0.9969
Stress(GPa)
Strain(%)
CPC-SP46 E=2.87 GPa
CPC-SP47 E=2.43 GPa
CPC-SP48 E=5.92 GPa
CPC-SP49 E=2.67 GPa
CPC-SP50 E=3.59 GPa
Linear (CPC-SP46 E=2.87 GPa)
Linear (CPC-SP47 E=2.43 GPa)
Linear (CPC-SP48 E=5.92 GPa)
Linear (CPC-SP49 E=2.67 GPa)
Linear (CPC-SP50 E=3.59 GPa)

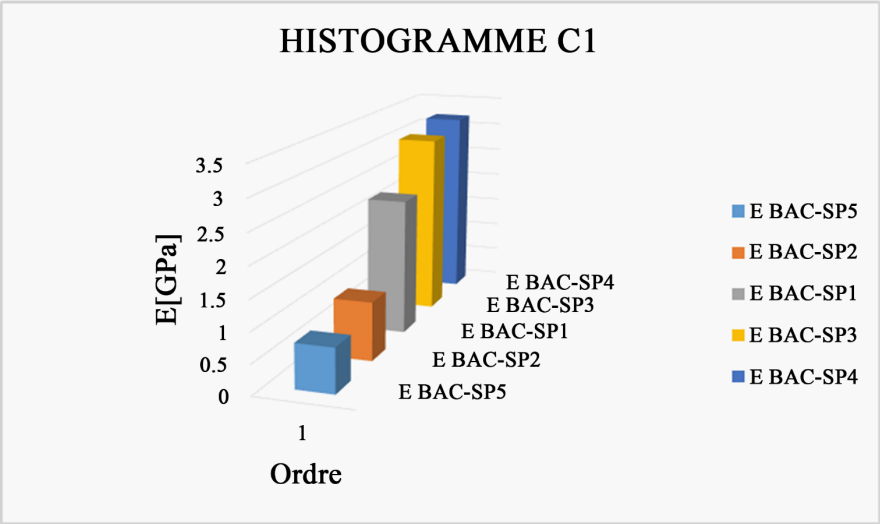
HISTOGRAMME C1
E[GPa]
3.5
3
2.5
2
1.5
1
0.5
0
1
Ordre
E BAC-SP4
E BAC-SP3
E BAC-SP1
E BAC-SP2
E BAC-SP5
E BAC-SP5
E BAC-SP2
E BAC-SP1
E BAC-SP3
E BAC-SP4

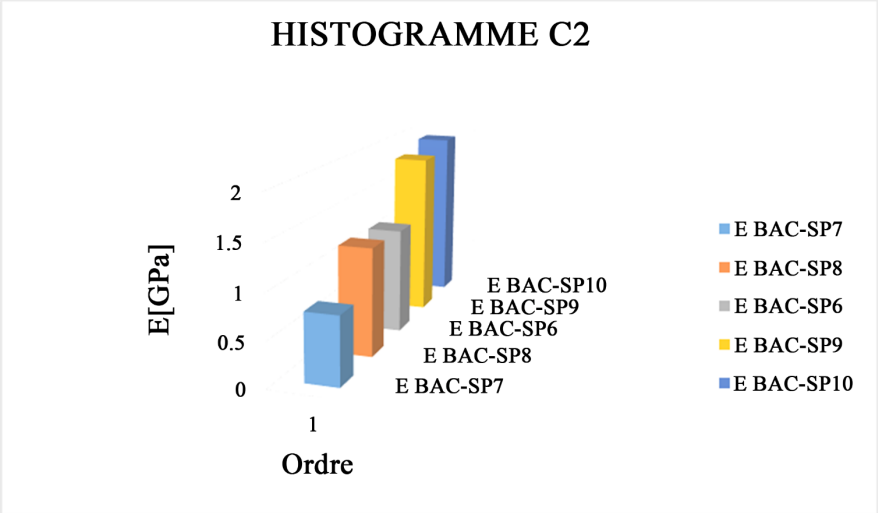
HISTOGRAMME C2
E[GPa]
2
1.5
1
0.5
0
1
Ordre
E BAC-SP10
E BAC-SP9
E BAC-SP6
E BAC-SP8
E BAC-SP7
E BAC-SP7
E BAC-SP8
E BAC-SP6
E BAC-SP9
E BAC-SP10

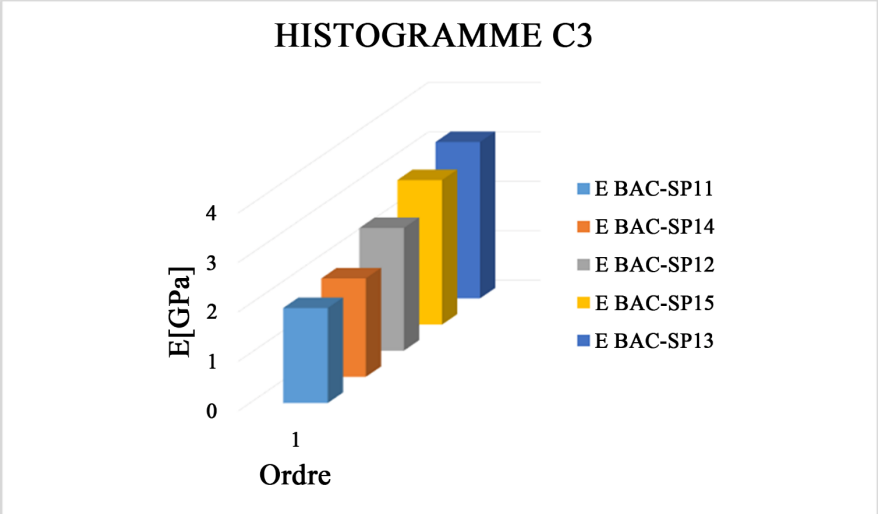
HISTOGRAMME C3
E[GPa]
4
3
2
1
0
1
Ordre
E BAC-SP11
E BAC-SP14
E BAC-SP12
E BAC-SP15
E BAC-SP13

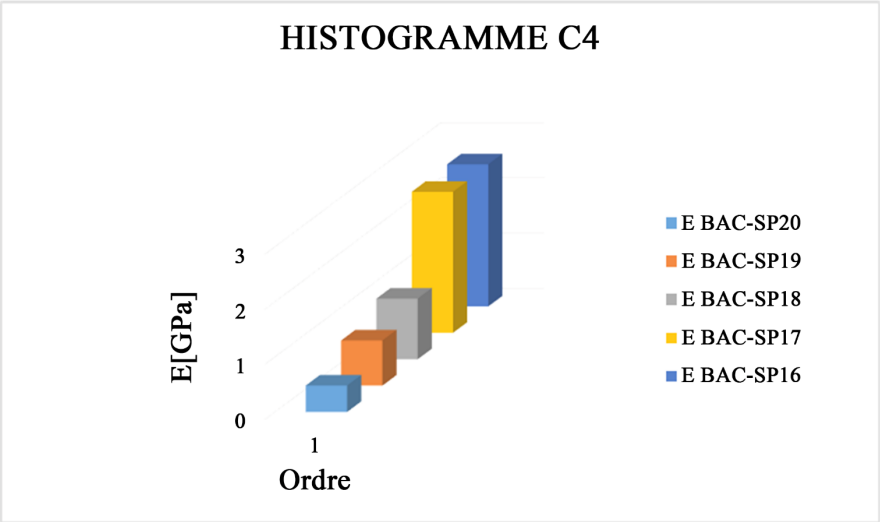
HISTOGRAMME C4
E[GPa]
3
2
1
0
1
Ordre
E BAC-SP20
E BAC-SP19
E BAC-SP18
E BAC-SP17
E BAC-SP16

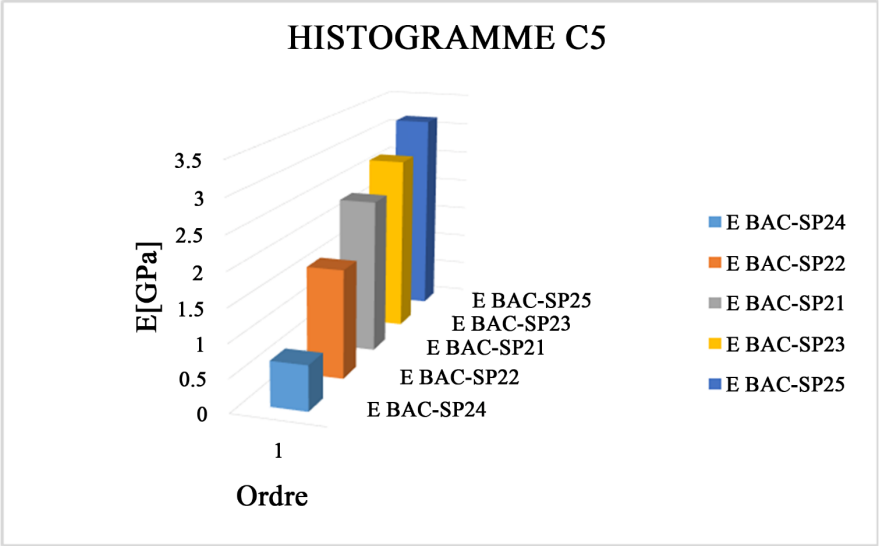
HISTOGRAMME C5
E[GPa]
3.5
3
2.5
2
1.5
1
0.5
0
1
Ordre
E BAC-SP25
E BAC-SP23
E BAC-SP21
E BAC-SP22
E BAC-SP24
E BAC-SP24
E BAC-SP22
E BAC-SP21
E BAC-SP23
E BAC-SP25

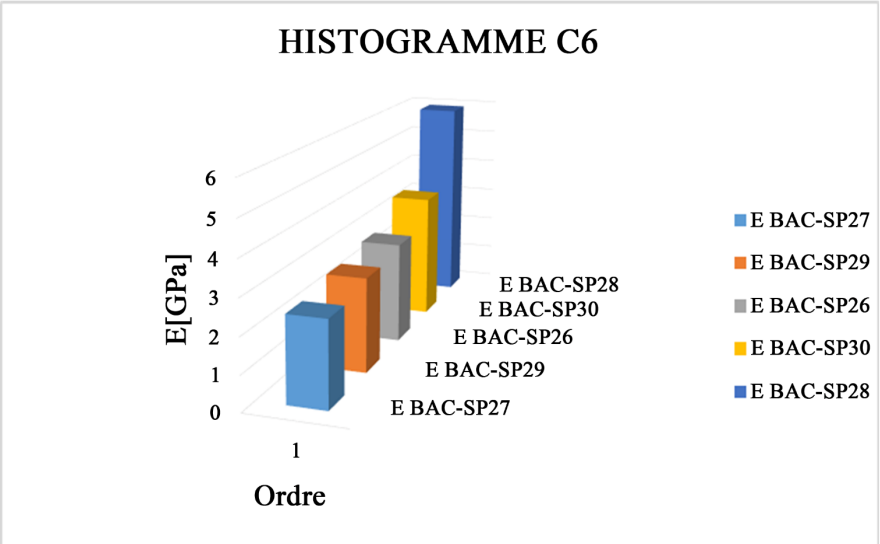
HISTOGRAMME C6
E[GPa]
6
5
4
3
2
1
0
1
Ordre
E BAC-SP28
E BAC-SP30
E BAC-SP26
E BAC-SP29
E BAC-SP27
E BAC-SP27
E BAC-SP29
E BAC-SP26
E BAC-SP30
E BAC-SP28

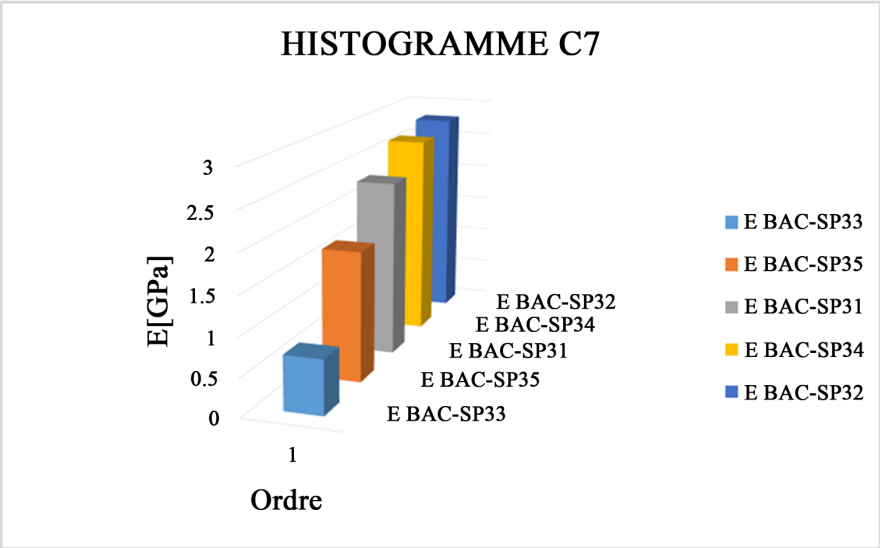
HISTOGRAMME C7
E[GPa]
3
2.5
2
1.5
1
0.5
0
1
Ordre
E BAC-SP33
E BAC-SP35
E BAC-SP31
E BAC-SP34
E BAC-SP32
E BAC-SP33
E BAC-SP35
E BAC-SP31
E BAC-SP34
E BAC-SP32

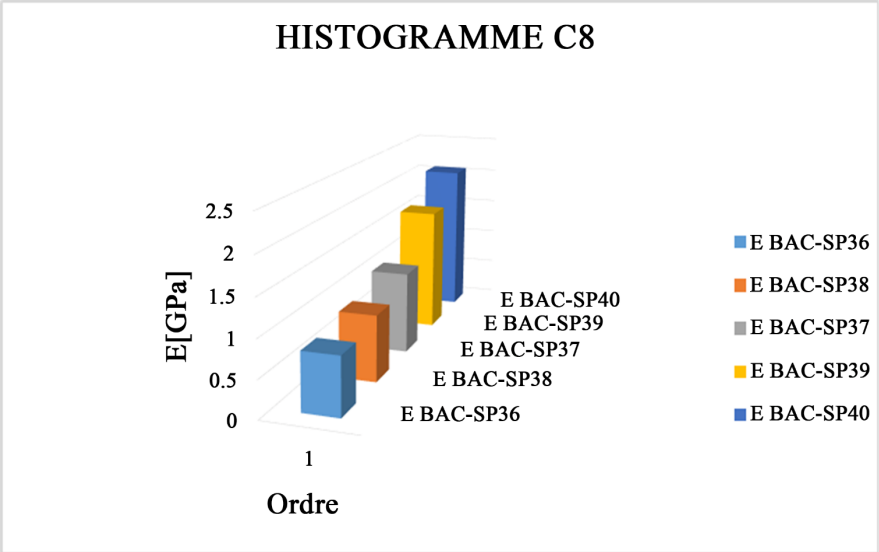
HISTOGRAMME C8
E[GPa]
2.5
2
1.5
1
0.5
0
1
Ordre
E BAC-SP36
E BAC-SP38
E BAC-SP37
E BAC-SP39
E BAC-SP40
E BAC-SP36
E BAC-SP38
E BAC-SP37
E BAC-SP39
E BAC-SP40

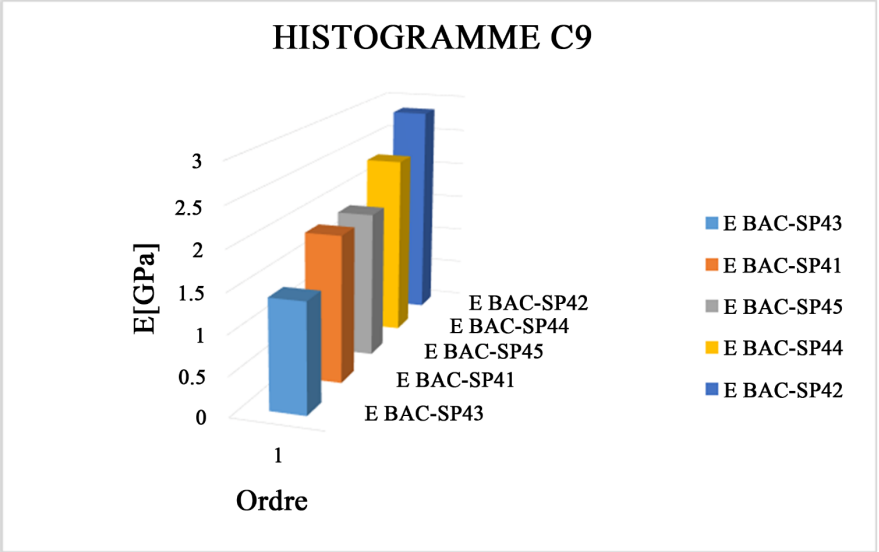
HISTOGRAMME C9
E[GPa]
3
2.5
2
1.5
1
0.5
0
1
Ordre
E BAC-SP43
E BAC-SP41
E BAC-SP45
E BAC-SP44
E BAC-SP42
E BAC-SP43
E BAC-SP41
E BAC-SP45
E BAC-SP44
E BAC-SP42

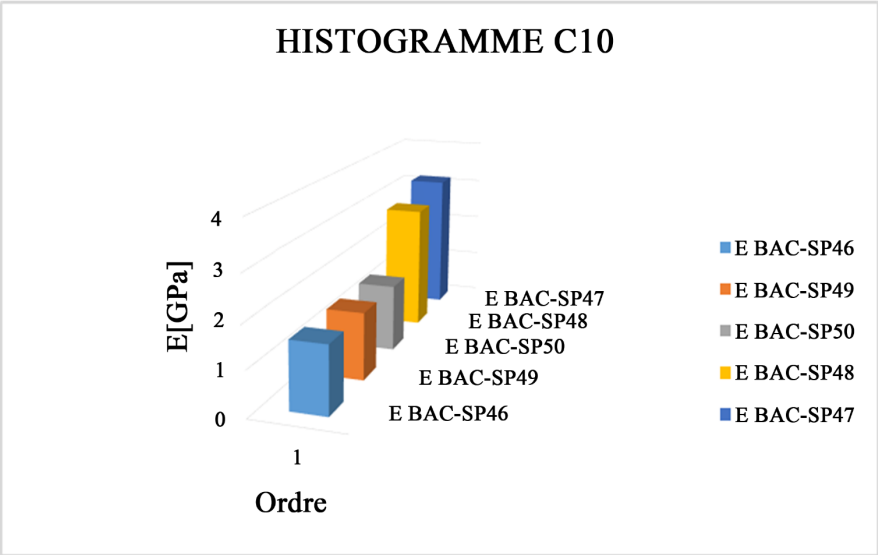
HISTOGRAMME C10
E[GPa]
4
3
2
1
0
1
Ordre
E BAC-SP47
E BAC-SP48
E BAC-SP50
E BAC-SP49
E BAC-SP46
E BAC-SP46
E BAC-SP49
E BAC-SP50
E BAC-SP48
E BAC-SP47

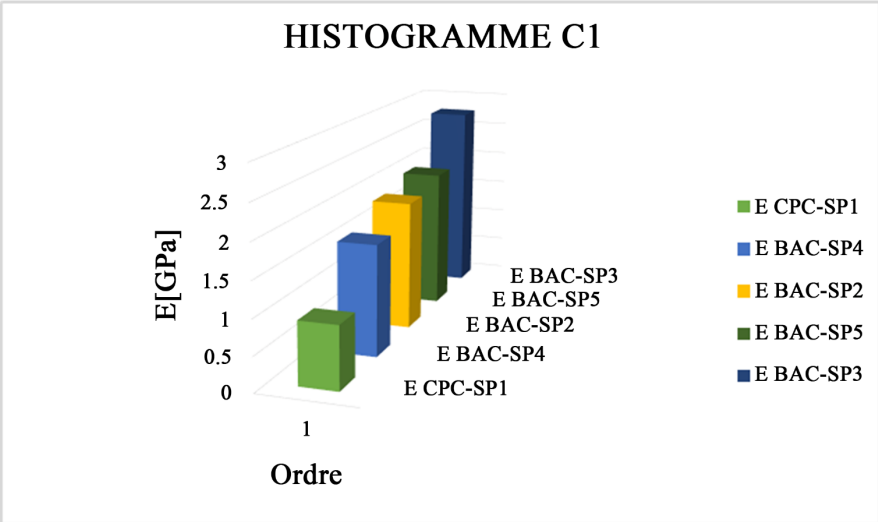
HISTOGRAMME C1
E[GPa]
3
2.5
2
1.5
1
0.5
0
1
Ordre
E BAC-SP3
E BAC-SP5
E BAC-SP2
E BAC-SP4
E CPC-SP1
E CPC-SP1
E BAC-SP4
E BAC-SP2
E BAC-SP5
E BAC-SP3

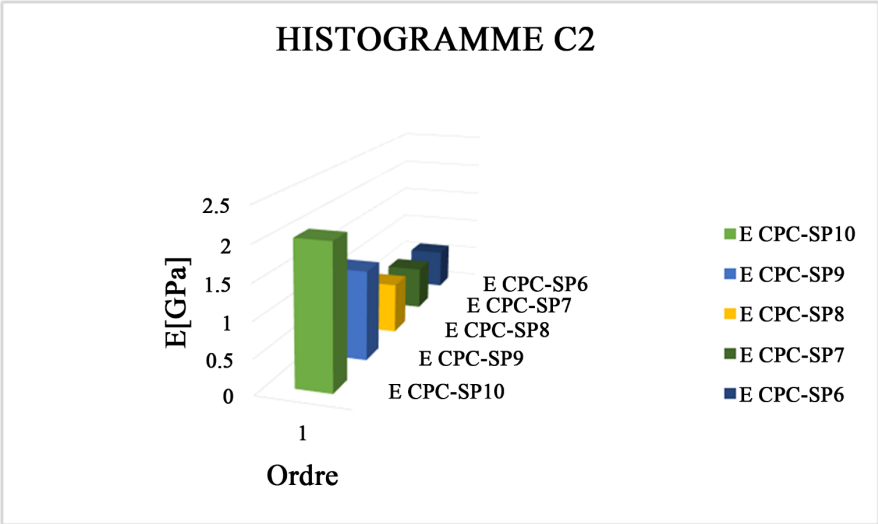
HISTOGRAMME C2
E[GPa]
2.5
2
1.5
1
0.5
0
1
Ordre
E CPC-SP6
E CPC-SP7
E CPC-SP8
E CPC-SP9
E CPC-SP10
E CPC-SP10
E CPC-SP9
E CPC-SP8
E CPC-SP7
E CPC-SP6

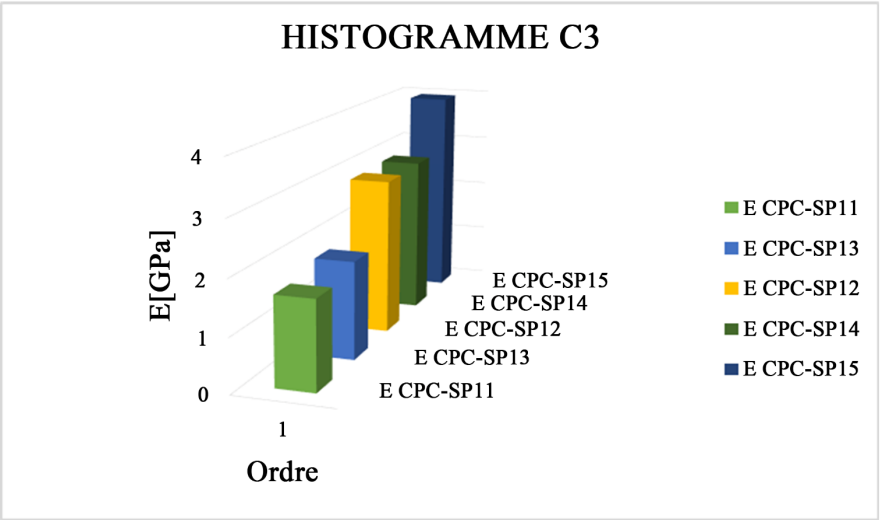
HISTOGRAMME C3
E[GPa]
4
3
2
1
0
1
Ordre
E CPC-SP15
E CPC-SP14
E CPC-SP12
E CPC-SP13
E CPC-SP11
E CPC-SP11
E CPC-SP13
E CPC-SP12
E CPC-SP14
E CPC-SP15

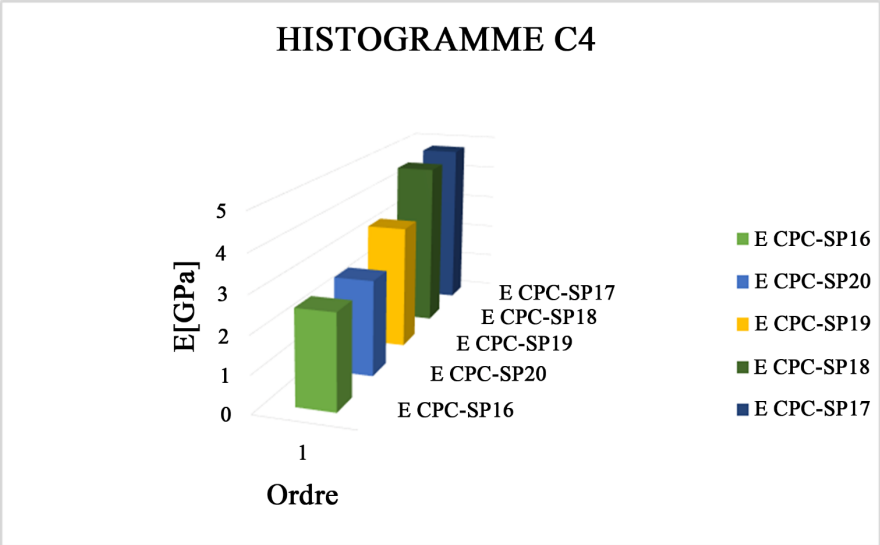
HISTOGRAMME C4
E[GPa]
5
4
3
2
1
0
1
Ordre
E CPC-SP17
E CPC-SP18
E CPC-SP19
E CPC-SP20
E CPC-SP16
E CPC-SP16
E CPC-SP20
E CPC-SP19
E CPC-SP18
E CPC-SP17

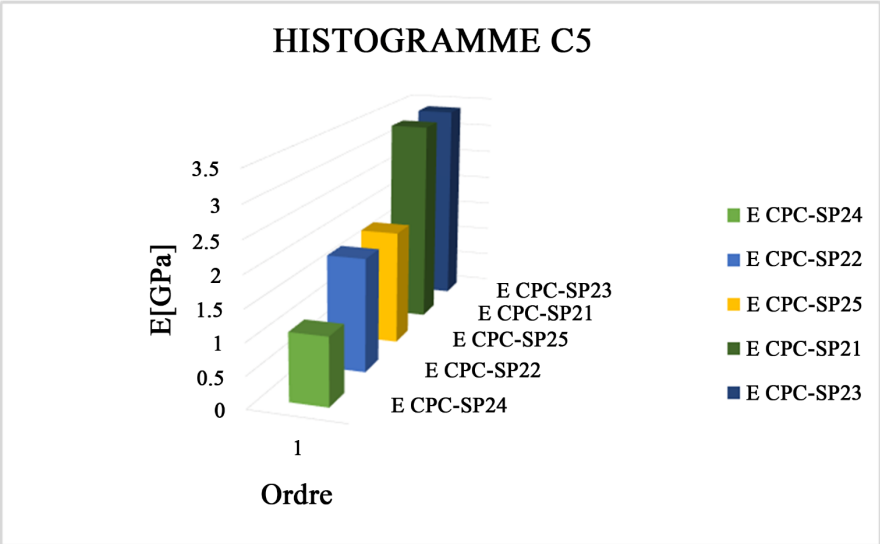
HISTOGRAMME C5
E[GPa]
3.5
3
2.5
2
1.5
1
0.5
0
1
Ordre
E CPC-SP23
E CPC-SP21
E CPC-SP25
E CPC-SP22
E CPC-SP24
E CPC-SP24
E CPC-SP22
E CPC-SP25
E CPC-SP21
E CPC-SP23

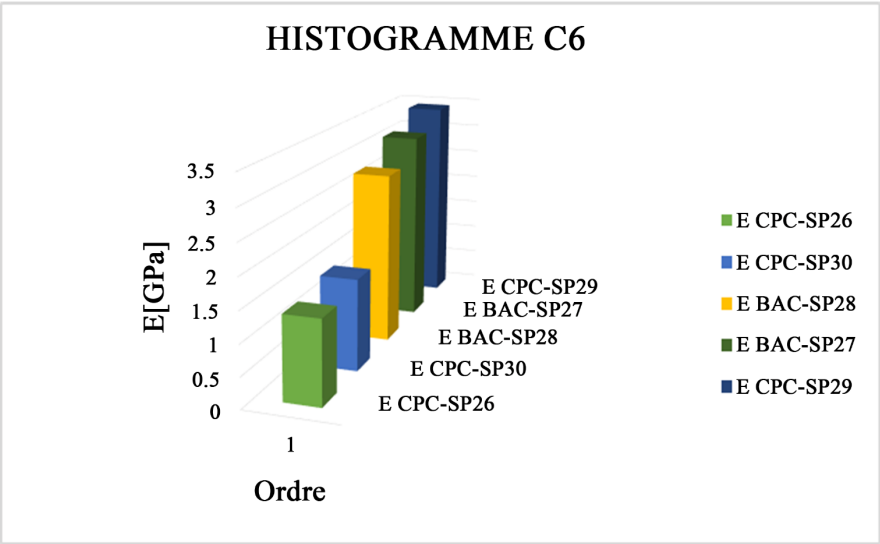
HISTOGRAMME C6
E[GPa]
3.5
3
2.5
2
1.5
1
0.5
0
1
Ordre
E CPC-SP29
E BAC-SP27
E BAC-SP28
E CPC-SP30
E CPC-SP26
E CPC-SP26
E CPC-SP30
E BAC-SP28
E BAC-SP27
E CPC-SP29

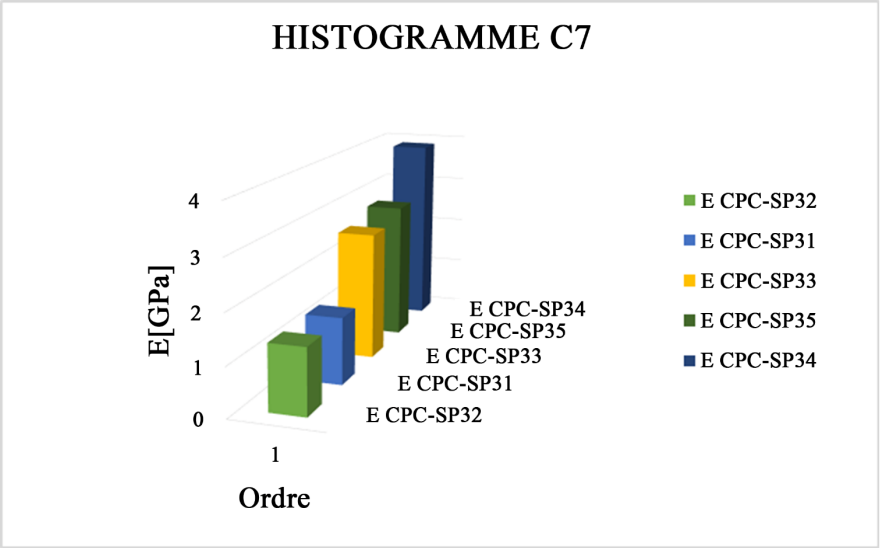
HISTOGRAMME C7
E[GPa]
4
3
2
1
0
1
Ordre
E CPC-SP34
E CPC-SP35
E CPC-SP33
E CPC-SP31
E CPC-SP32
E CPC-SP32
E CPC-SP31
E CPC-SP33
E CPC-SP35
E CPC-SP34

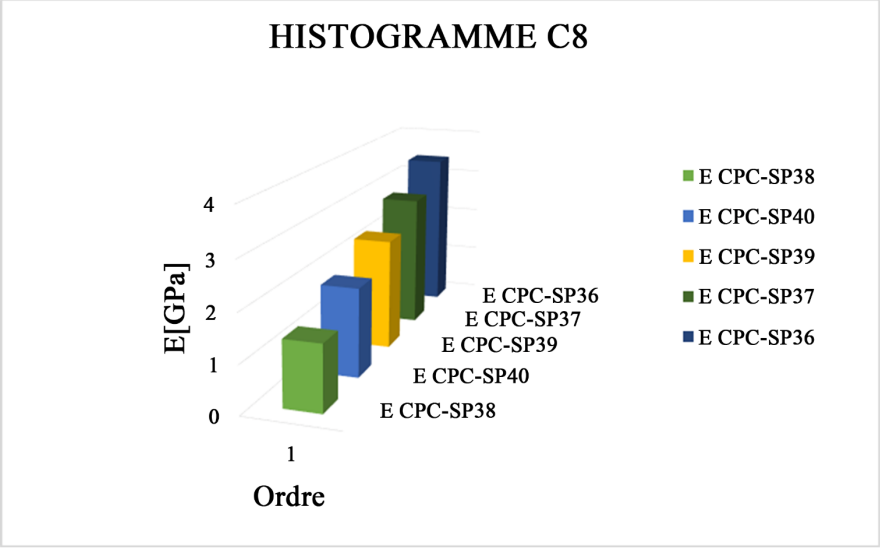
HISTOGRAMME C8
E[GPa]
4
3
2
1
0
1
Ordre
E CPC-SP36
E CPC-SP37
E CPC-SP39
E CPC-SP40
E CPC-SP38
E CPC-SP38
E CPC-SP40
E CPC-SP39
E CPC-SP37
E CPC-SP36

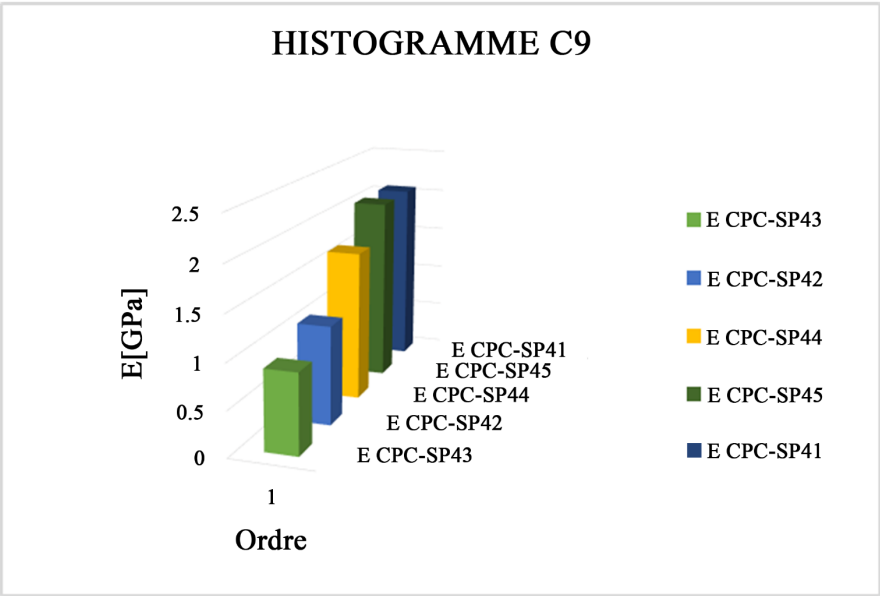
HISTOGRAMME C9
E[GPa]
2.5
2
1.5
1
0.5
0
1
Ordre
E CPC-SP41
E CPC-SP45
E CPC-SP44
E CPC-SP42
E CPC-SP43
E CPC-SP43
E CPC-SP42
E CPC-SP44
E CPC-SP45
E CPC-SP41

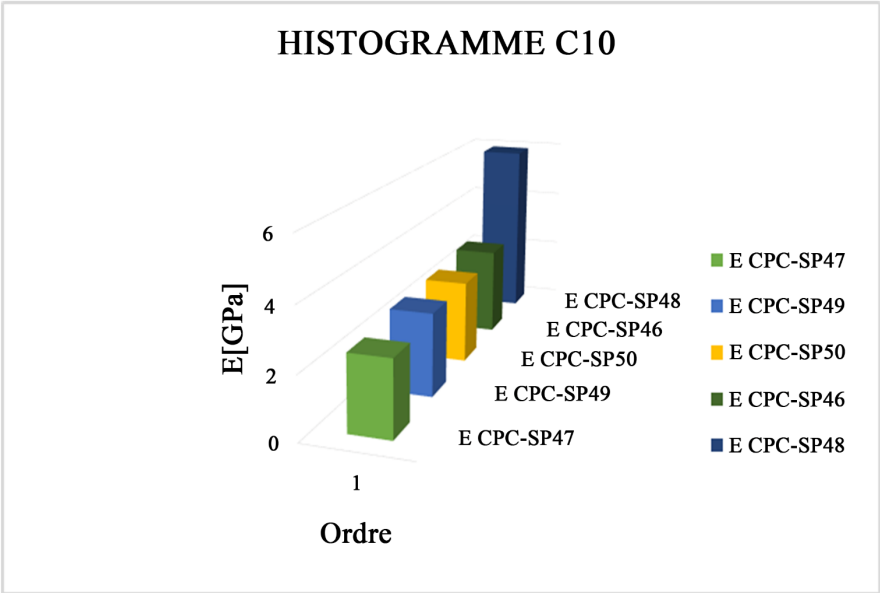
HISTOGRAMME C10
E[GPa]
6
4
2
0
1
Ordre
E CPC-SP48
E CPC-SP46
E CPC-SP50
E CPC-SP49
E CPC-SP47
E CPC-SP47
E CPC-SP49
E CPC-SP50
E CPC-SP46
E CPC-SP48